GEN-289

~~S. K. Ottesen – 8313~~
~~G. C. Zuppero – 8342~~

COO-2888-2

ENERGY
CONSERVATION

MOLTEN SALT THERMAL ENERGY STORAGE SYSTEMS: SYSTEM DESIGN

February 1977

Work Performed Under Contract No. EY-76-C-02-2888

Institute of Gas Technology
Chicago, Illinois

ENERGY RESEARCH AND DEVELOPMENT ADMINISTRATION

Division of Energy Storage Systems

④

NOTICE

Available from the National Technical Information Service, U. S. Department of Commerce, Springfield, Virginia 22161

Price: Paper Copy $5.00 (domestic)
$7.50 (foreign)
Microfiche $3.00 (domestic)
$4.50 (foreign)

COO-2888-2
Distribution Category UC-94a

MOLTEN SALT THERMAL ENERGY STORAGE SYSTEMS: SYSTEM DESIGN

Project 8981 Topical Report

H. C. Maru
A. Kardas
V. M. Huang
J. F. Dullea
L. Paul
L. G. Marianowski

Prepared by

Institute of Gas Technology
IIT Center, 3424 S. State Street
Chicago, Illinois 60616

February 1977

Under Contract No. EY-76-C-02-2888
(Original Contract No. E(11-1)-2888)

Prepared for the

ENERGY RESEARCH
AND
DEVELOPMENT ADMINISTRATION

TABLE OF CONTENTS

TABLE OF CONTENTS (Cont.)

LIST OF FIGURES

LIST OF FIGURES, Cont.

LIST OF TABLES

ABSTRACT

A five-task research program aimed at the development of molten salt thermal energy storage systems commenced in June 1976. The first topical report, covering Task 1, the selection of suitable salt systems for storage at 850° to 1000°F, was issued in August 1976. We concluded that a 35 weight percent Li_2CO_3-65 weight percent K_2CO_3 ($LiKCO_3$) mixture was most suitable for the purpose. The present topical report, covering Task 2, describes our work on system design considerations.

Interrelationships between various design parameters were examined using the available solutions, and an engineering-scale storage unit was designed. This unit has an annular configuration with a 1-foot OD, 1.5-foot high, 2-inch diameter heat transfer well. Preliminary experiments on a pilot size (3-inch OD) unit showed that temperature profiles and progress of the solid-liquid interface agreed with those predicted theoretically. Also, no supercooling was observed during cooldown, and the presence of significant convective mixing was indicated by negligible temperature gradients. Convective mixing is desirable because it allows higher heat transfer rates than those possible if the heat is transferred solely by conduction. Volume change for the $LiKCO_3$ system was estimated to be $\sim 10\%$ between room temperature and the upper operating temperature. Use of a lithium aluminate volume-change suppressor was investigated, but it appears to be nonessential because of the low volume-change in the $LiKCO_3$ system. Our consideration of the relative heat-transfer resistances under practical conditions suggested that the use of a conductivity promoter will enhance the heat-transfer rates, thereby requiring smaller heat-transfer areas. Different configurations and materials were considered for this application; an aluminum wool appears to be most suitable. We also investigated the corrosion resistance of various construction materials; stainless steels and aluminum appear to be suitable construction materials for carbonates in the 850° to 1000°F range.

Testing of the engineering-scale system (Task 3) and verification of the conclusions derived under Task 2 are in progress at the present time.

OBJECTIVE AND SCOPE OF WORK

The objective of this work is to determine the feasibility of using a mixture of carbonate salts to store thermal energy by utilizing, primarily, the enthalpy change (heat-of-fusion) occurring at the melting point of the mixture in the temperature range of 850^0 F to 1000^0 F.

The work includes –

Task 1. The selection of a carbonate mixture

Task 2. The formulation of the heat exchange and storage equations governing the thermal fluxes, and parametric analysis using these equations to determine the effects of using inert supports to contain the carbonates and conductivity enhancers to improve the thermal conductivity of the carbonates

Task 3. Design and operation of engineering-scale thermal energy storage systems (TES) to –

a. Verify the model analytical thermal equations derived and validate the use of inert supports and conductivity promoters

b. Provide "first-cut" engineering data required for the design of prototype thermal energy storage hardware

Task 4. Evaluation and analysis of the data generated

Task 5. Recommendations for further work.

The work on Task 1 was completed in June 1976, and a topical report was published. The work on Task 2 is presented in this topical report. Task 3 is in progress, and the work on Tasks 4 and 5 has not been initiated.

DETAILED DESCRIPTION OF TECHNICAL PROGRESS: TASK 2. SYSTEM DESIGN

2.1. SUMMARY

This topical report is devoted to the discussion of work performed under Task 2, System Design. Under Task 1 of this program we investigated several inorganic salts for their suitability as phase-change thermal energy storage materials in the range of 850° to 1000°F. We selected a 35 weight percent Li_2CO_3-65 weight percent K_2CO_3 mixture ($LiKCO_3$) as a model system. Under Task 2 we have studied —

1. Heat transfer characteristics of phase-change storage systems to determine interrelationships between various design parameters, and to provide methodology for design and optimization of the phase-change thermal energy storage system.
2. Use of volume-control additives to minimize void formation resulting from volume changes accompanying the phase change.
3. Use of conductivity promoters to improve heat transfer rates.
4. Possible construction materials for containment, heat transfer surfaces, and the conductivity promoter.

Our progress on these tasks is summarized below.

- Because of the complexities involved in phase-change thermal energy storage, only a limited number of approximate solutions are available for heat-transfer analysis. We have utilized these solutions to elucidate the relationships between various factors involved in system design. An "apparent heat capacity" concept to account for sensible and latent heat allowed use of conventional heat-transfer solutions. Using these solutions we have designed the engineering-scale unit for further studies. This unit is a 1-foot-diameter cylinder 1.5-feet tall, with an internal heating and cooling tube of 2-inch diameter. Design considerations suggest that, under practical operating conditions, heat transfer resistance on the salt side is rate-limiting and that further improvements in overall heat transfer rates can be achieved by the use of conductivity promoters.

  Formulation of a general computer model to simulate the engineering-scale unit was also initiated during the reporting period.

- Preliminary experimental studies have been performed in a 3-inch diameter pilot unit to verify the assumptions made in the heat transfer analysis. Results from these studies showed that:

1. Convective mixing occurred in the liquid portion of the salt, so the temperature distribution was uniform in the liquid portion. Relatively faster heat transfer rates are expected because of this convective mixing. This observation also allowed the use of simple solutions for heat transfer analysis.

2. No supercooling was observed during cooldown. This ideal behavior is an advantage compared with the low temperature phase change systems (such as Glauber's salt), where significant supercooling is observed, and additives or system modifications are required to minimize supercooling.

3. Temperature profiles and the progress of the solid-liquid interface (freezing front) agreed reasonably well with those predicted from the approximate solutions.

- The melting behavior of our model system was verified using DTA measurements, which confirmed the melting point reported in the literature. Some supercooling was observed at slow cooling rates, but no supercooling was observed at cooling rates comparable to those expected in the TES system. The volume change accompanying the phase change of $LiKCO_3$ was estimated using thermal expansion measurements on solid pellets and a published value of the liquid density. The volume change on melting was estimated to be $\sim 5\%$ and the total volume change from room temperature to the upper operating temperature was estimated to be $\sim 10\%$.

- The suitability of a lithium aluminate material, developed at the Institute of Gas Technology for fuel cell applications, was investigated as a volume-change suppressor. A volume-change suppressor may be advantageous, because it can minimize the formation of large voids during cooling that may hinder the heat transfer. Lithium aluminate was selected for this purpose because its stability in the Li_2CO_3-K_2CO_3 system has already been established. Our measurements of settling rates showed that a small amount of settling can be expected because of the density differences. The addition of the volume-change suppressor also results in penalties in terms of storage capacity and material cost. Because our $LiKCO_3$ system shows very low volume change, the use of a volume-change suppressor is judged unimportant, but the concept of volume-change suppression may be useful for other salts with large volume changes upon melting.

- Several materials and configurations were investigated as conductivity promoters. Our experiments in the pilot TES unit showed that aluminum wool may be the most suitable candidate. This configuration is also advantageous because it provides some volume-change control by localizing the void formation in small capillaries in its structure. Further experimental studies in our pilot TES system are in progress, and this material will also be tested in our engineering-scale unit.

- Available data on corrosion of construction materials were compiled, and preliminary corrosion measurements were made on the materials used for the experiments described above. Aluminum and the 300-series stainless steels appear to be suitable construction materials up to 1000°F.

2.2. HEAT TRANSFER STUDIES

The objectives of this subtask are:

1. To determine interrelationships between various factors affecting energy storage and to estimate the relative magnitudes of various heat transfer resistances and the overall heat transfer flux, and
2. to develop the mathematics and methodology required to aid in design of phase-change thermal energy storage systems.

After such an analysis is developed and its viability proven in the laboratory, accurate design and cost estimates can be made to determine the feasibility of storing thermal energy in phase change materials (PCM).

Heat transfer analysis of a PCM storage system presents two major complexities –

1. Heat is stored in a PCM in the form of latent heat and sensible heat, and the solid-liquid interface moves during the transfer of heat.
2. Because of the regenerative nature of the storage system, a cyclic solution needs to be considered.

Due to these complexities, only a limited number of approximate solutions have been obtained in the past. We have utilized these solutions, with suitable modifications, to establish interrelationships between different variables and for the design of our experimental system. To more closely simulate the behavior of the PCM storage system, we have also formulated a numerical solution that takes into account sensible and latent heat and the cyclic operation of the storage unit. In the following sections, we will discuss the background, a brief review of the past work, observed interrelationships between variables of interest, experimental verification of some approximations, design of the experimental unit using the approximate solutions and finally the formulation of the numerical solution.

2.2.1. Background and Past Work

2.2.1.1. Basic Equations in Phase Change Heat Transfer

A regenerative heat-storage-and-retrieval system comprises a finite mass of storage material and two "working fluids." One of these supplies some of its heat content to storage and the other transfers the stored thermal energy from the TES. Because in our case the storage material undergoes a phase change, both the liquid and solid phase are present in the unit, and the solid-liquid interface moves during the transfer of heat. A schematic of the temperature profile in such a system is shown in Figure 2.2.1. Because the heat capacities and conductivities of the two phases are different and the boundary between the two phases is not fixed in space, the mathematical analysis of heat transfer requires simultaneous consideration of both phases with an appropriate boundary condition. Thus, in the solid phase the heat flow follows Fourier's law of heat conduction –

$$\frac{1}{\alpha_s} \frac{\partial t_s}{\partial \tau} = \text{div grad } t_s \tag{2.2.1}$$

In the liquid phase, in the absence of convective currents, the heat flow can be described by

$$\frac{1}{\alpha_\ell} \frac{\partial t_\ell}{\partial \tau} = \text{div grad } t_\ell \tag{2.2.2}$$

At the moving interface, the heat is absorbed in the form of latent heat of fusion, so that

$$k_s \text{ grad } t_s - k_\ell \text{ grad } t_\ell = \rho \, \Delta H_f \frac{\partial X}{\partial \tau} \tag{2.2.3}$$

and

$$t_s = t_\ell = t_m \tag{2.2.4}$$

where

t = temperature

α = thermal diffusivity

τ = time

k = thermal conductivity

ΔH_f = latent heat of fusion

ρ = density of the salt (assumed approximately equal for liquid and solid phases)

X = position of the moving interface.

Subscripts s and ℓ refer to solid and liquid phases and subscript m refers to melting point of the salt. The heat transferred to the working-fluid is given by

$$c_{pf} \rho_f \frac{Dt_f}{D\tau} = -U \left(\frac{A}{V}\right) (t_f - t_w) \qquad (2.2.5)$$

which is coupled by the relation

$$k \text{ grad } t = U (t_w - t_f) \qquad (2.2.6)$$

at the wall of the heat transfer conduit. Solutions of the system of Equations 2.2.1, 2.2.2, and 2.2.6 exist only for a few selected geometries with additional simplications introduced to make the solution process tractable.

Additional complexities are involved because of the periodic nature of the storage-retrieval cycle. If the same fluid is used in the heating and cooling half cycles, the inlet temperature, $t_{f,\ in}$, can be represented by a periodic function, such as

$$t_{f,in} = 1/2 \left[t_{hot} + t_{cold} + (t_{hot} - t_{cold}) \cos \omega\tau \right] \qquad (2.2.7)$$

where

t_{hot} = maximum temperature of the hot stream

t_{cold} = minimum temperature of the cold stream

ω = frequency

For a more general case, a Fourier series summing the individual harmonics of Equation 2.2.7 can be used to construct actual temperature variation in $t_{f,\ in}$.

2.2.1.2. Solutions for Phase Change Heat Transfer

The available analytical solutions can be classified in two categories —

1. Transient (noncyclic) solutions that assume an initially uniform temperature profile
2. Cyclic solutions that account for the regenerative nature of the storage system.

The transient solutions are useful for experimental studies because a) the heat transfer coefficients can be determined or verified by recording the time-dependent temperature behavior of the working fluids, and b) heating of energy storage materials past the phase change and into the liquid phase results in starting the solidification half cycle at an approximately uniform temperature. We have found experimentally, and the hydrodynamic stability theory also suggests, that a temperature gradient in the liquid phase of the reference salt cannot be maintained in a layer more than a fraction of an inch thick. This means that the solidification half cycle can be studied analytically using transient solutions in several geometrical configurations.

Periodic solutions are important for storage system design, but no such solutions involving phase change are known in the literature. However, useful information can be obtained using the available solutions for regenerative heat transfer in sensible heat storage materials.

Solutions of both categories are briefly described below. Applications of these solutions to determine interrelationships between various parameters are discussed subsequently.

2.2.1.2.1. Transient Solutions

An approximate solution to two-phase heat transfer can be obtained if sensible heat is assumed to be negligible compared with latent heat, and if a perfect contact assumed between the coolant and the solid storage material. For a flat plate geometry (Figure 2.2.2), let the solid storage material at $x = a$ advancing with velocity, v, into the liquid phase move through the distance δa in time $\delta \tau$, so that $\delta a = v\, \delta \tau$.

The latent heat released by a unit-area interface in time $\delta \tau$ is $q = \rho\, \Delta H_f\, v\, \delta \tau$, in Btu. This amount of energy is conducted across the solid phase and transferred to the **coolant** at $x = 0$, where $q = -k \operatorname{grad} t \cdot \delta \tau$. Approximating grad t by $(t_a - t_m)/a$, we have

$$\rho\, \Delta H_f\, v d\tau = \rho\, \Delta H_f\, da = k(t_m - t_a)\, \delta \tau / a \qquad (2.2.8)$$

and, upon integrating,

$$0.5\, a^2 = \frac{k\, \tau (t_m - t_a)}{\rho\, \Delta H_f} \qquad (2.2.9)$$

or in dimensionless form,

$$N_{Fo} = 0.5\, N_{ph} \tag{2.2.10}$$

where

N_{Fo} = Fourier number = $\frac{k}{c_p \rho} \frac{\tau}{a^2}$, and

N_{ph} = Phase change number = $\frac{\Delta H_f}{c_p (t_m - t_a)}$

In a hollow cylinder with $R = r/r_o$, where r_o is the radius at which the coolant is in contact with the solid, a similar analysis leads to

$$N_{Fo} = 0.5\, N_{ph} \left(R^2 \ln R + \frac{1-R^2}{2} \right) \tag{2.2.11}$$

$R \le 1$ in cooling from outside; $R \ge 1$ in cooling from inside. Bramlette et al.[1] used these approximate solutions to compare heat fluxes among different containment configurations, and inferred that an annular arrangement (working fluid inside) would provide the best heat fluxes.[1] The assumptions involved in the heat balance, namely $c_p \rightarrow 0$ and $U \rightarrow \infty$ are not general. A check against a solution (to be discussed below) that does not resort to these assumptions showed that N_{Fo}, as calculated from Equation 2.2.11, was off by a factor of 2 to 3 for N_{ph} values between 0.5 and 10, using $N_{Bi} = Ur_o/k_s = 1$. Thus use of the approximations stated above is not recommended for design of the storage unit.

A more realistic model must include a finite heat transfer coefficient, h, at the boundary, and conductance, k, across the wall, i.e., $U = \left(\frac{1}{h} + \frac{d}{k}\right)^{-1}$. No assumptions should be made on the nature of the temperature profile in the solid phase, i.e., a finite sensible heat of the solid phase should be included.

Such an analysis was performed by Megerlin.[2] In his solution, the time-dependent trial functions appear as coefficients in a power-series expansion of the depth coordinate. The trial functions are determined by recursion from a set of ordinary differential equations that arise when the power series expansion is operated on by the partial differential equations and the constraints defining the problem.

Two relevant results are given below. Equation 2.2.12 represents the velocity with which the freezing front in a hollow cylinder moves from the inside radius r_o outward. N_{Fo} and N_{Bi} are based on the inside radius and $r^* = r_{interface}/r_o$.

$$\frac{dr^*}{dN_{Fo}} = \frac{-(N_{Bi}\ln r^*+1)+\sqrt{(N_{Bi}\ln r^*+1)^2+2\,\frac{N_{Bi}}{N_{ph}}\ln r^*(N_{Bi}\ln r^*+2)}}{r^*\ln r^*(N_{Bi}\ln r^*+2)} \qquad (2.2.12)$$

Equation 2.2.13 gives the dimensionless time needed to solidify the molten material from $r^*=1$ to $r^*=R$.

$$N_{Fo} = \int_1^R \frac{r^*\ln r^*(N_{Bi}\ln r^*+2)\,dr^*}{\sqrt{(N_{Bi}\ln r^*+1)^2+2\,\frac{N_{Bi}}{N_{ph}}\ln r^*(N_{Bi}\ln r^*+2)}-(N_{Bi}\ln r^*+1)} \qquad (2.2.13)$$

Solved for the solidified layer thickness R, measured in terms of the internal radius r_o, Equation 2.2.13 yields the thickness of the solid-phase layer as a function of time. Two illustrative results obtained by evaluating the integral in Equation 2.2.13, numerically are shown in Figure 2.2.3. The family of curves with phase number $N_{ph}=0.57$ describes the solid layer thickness of the reference material cooled with room temperature air.† Phase change number $N_{ph} = 10$ refers to the same material with the coolant running only about 25°C colder than the melting temperature of the salt.

---

† For illustrative purposes, we have used properties of the salt system $LiKCO_3$ selected for our experimental work. Relevant thermophysical properties of this system are[3] –

Composition: 35 weight percent Li_2CO_3 - 65 weight percent K_2CO_3 ($LiKCO_3$)
Melting Point: 941°F (505°C)
Heat of fusion (ΔH_f): 148 Btu/lb_m
Heat Capacity at melting point: $c_{ps}=0.32$, $c_{p\ell}=0.42$ Btu/lb - °F
Thermal Conductivity at melting point: $k_s=1.3$, $k_\ell=1.09$ Btu/hr-ft-°F
Viscosity at Melting Point plus 50°F: $\mu=15$ cP
Density at 25°C: $\rho = 141.5$ lb_m/cu ft
Density at Melting Point: $\rho_\ell = 125.4$ lb_m/cu ft.

These curves can be used to calculate various parameters, such as time required to solidify a given core of PCM, effect of heat transfer coefficient, coolant temperature, and conductivity promoters. For example, if coolant air is only approximately 25°C cooler than the melting point of the PCM ($N_{ph} = 10$) the time required for solidifying a given layer of salt would be approximately 10 times greater than that required if room-temperature air is used ($N_{ph} = 0.57$). On the other hand, if time is kept fixed, say $N_{Fo} = 10$, the thickness of the layer r* should be reduced by half. Similarly, the effect of the relative resistance of heat transfer on the heat-transfer-fluid side and the storage-medium side can be determined by observing the effect of the Biot number ($N_{Bi} = Ur_o/k_s$) on the thickness of the solidified layer. As can be observed from Figure 2.2.3, for $N_{ph} = 10$ and a fixed thickness of a given PCM, an increase in N_{Bi} from 0.5 to 5 results in a two-fold decrease in the time required, τ. A further increase in N_{Bi}, from 5 to 50, results in only a slight decrease in τ. This suggests that the heat transfer resistance in the solid storage material is limiting above $N_{Bi} > 5$. For $N_{Bi} \simeq 0.5$ (the range expected in our engineering-scale unit, Section 2.2.4), the heat transfer resistance in the PCM still appears to be the major factor, but the contribution of heat transfer on the heat-transfer-medium side is significant. If the conductivity k_s of the PCM is doubled, i.e., $N_{Bi} = 0.25$, the value of τ required to solidify a layer of R = 6 decreases to 75% of the original value. Further application of these curves will be presented in Section 2.2.4, where design of the experimental unit is discussed.

An analytical solution for a semi-infinite flat plate geometry was presented by Neumann,[4] who assumed the PCM initially at the melting point, t_m, no temperature gradient in the liquid phase, and the surface at $x = 0$ subsequently held at $t_a < t_m$. Equation 2.2.3 then becomes

$$k_s \text{ grad } t_s = \rho \Delta H_f \frac{dX}{d\tau} \qquad (2.2.14)$$

Because the moving interface at $x = X$ remains at constant temperature. t_m, the convective temperature derivative there, is zero,

$$\frac{Dt}{D\tau} = \frac{\partial t}{\partial \tau} + \frac{dX}{d\tau} \text{ grad } t = 0 \qquad (2.2.15)$$

Substituting $\frac{dX}{d\tau}$ from Equation 2.2.14, we obtain

$$\frac{\partial t}{\partial \tau} = \frac{-k}{\rho \Delta H_f} (\text{grad } t)^2 \tag{2.2.16}$$

The nonlinearity of the interface condition (Equation 2.2.16) precludes the use of classical methods in which enough particular solutions are added until field equations and the boundary and initial conditions are satisfied. Neumann, using the assumptions stated above, obtained a special analytical solution that provides a temperature profile in the solid phase as [4]

$$t(x,\tau) - t_a = \frac{t_m - t_a}{C} \text{ erf } \left(\frac{x}{2\sqrt{\alpha_s \tau}} \right) \tag{2.2.17}$$

where C is the coupling coefficient defined by the following equation,

$$C \exp C^2 \text{ erf } C = \frac{1}{\sqrt{\pi}\ N_{ph}} \tag{2.2.18}$$

By comparison, a solution of the same heat transfer problem not involving a phase change is

$$t(x, \tau) - t_a = (t_m - t_a) \text{ erf } \frac{x}{2\sqrt{\alpha\tau}} \tag{2.2.19}$$

It is interesting to note that this is the only exact analytic solution* for phase-change heat transfer known in the literature for more than 100 years. Neumann's solution is valuable because other methods can be checked against it.

2.2.1.2.2. Periodic Solutions

As mentioned earlier, no periodic solutions are available for phase change heat transfer. Therefore, we can consider a simple periodic solution for a flat plate, sensible heat system, and then introduce a concept of "apparent sensible heat" to account for latent heat and sensible heat simultaneously.

For a flat plate geometry, Equation 2.2.1 can be written as

$$\frac{\partial t}{\partial \tau} = \alpha \frac{\partial^2 t}{\partial x^2} \tag{2.2.20}$$

---

* Megerlin's solution, although applicable to phase-change heat-transfer, is a series solution assuming time dependent trial functions.

For a cyclic variation in the working-fluid temperature, the temperature in the PCM is given as

$$t(x, \tau) = A \exp[-x(1+i)K] \exp(i\omega\tau) \tag{2.2.21}$$

where

A = a constant
i = $\sqrt{-1}$
K = wave number, $\sqrt{\frac{\omega}{2\alpha}}$ or $\sqrt{\frac{\pi\nu}{\alpha}}$
ω = frequency, $2\pi\nu$

The thermal diffusivity $\alpha = k/c_p\rho$ can be modified by assuming an apparent c_p of a fictitious solid, which can be obtained as follows.

Heat released per unit mass, Q, by a PCM between temperatures t_m and t_a, having a heat capacity c_{ps} and latent heat ΔH_f is given as

$$Q = c_{ps}(t_m - t_a) + \Delta H_f \tag{2.2.22}$$

and for the fictitious solid with heat capacity, $c_{p,\,app}$, Q is given as

$$Q = c_{p,\,app}(t_m - t_a) \tag{2.2.23}$$

From these two equations,

$$c_{p,\,app} = c_{ps}\left[1 + \frac{\Delta H_f}{c_{ps}(t_m - t_a)}\right] \tag{2.2.24}$$

or, in terms of N_{ph},

$$c_{p,\,app} = c_{ps}[1 + N_{ph}] \tag{2.2.25}$$

Note that the value of $c_{p,\,app}$ is dependent on $\Delta t = t_m - t_a$ and is not purely a property of the PCM. Also, because during cooldown the entire mass of PCM does not attain temperature t_a, either an average temperature or the temperature of the working fluid can be used. When $N_{ph} \gg 1$,

$$c_{p,\,app} \approx c_{ps} \cdot N_{ph} = \frac{\Delta H_f}{t_m - t_a} \tag{2.2.26}$$

Using the properties of our storage material $LiKCO_3$, and $t_a = 72°F$ (22°C),

$$N_{ph} = 0.53$$

and $c_{p,\ app.}$ from Equation 2.2.25 is 0.49 Btu/lb-°F. Comparing Neumann's solution, Equation 2.2.17, with the no-phase change solution, Equation 2.2.19 suggests that an apparent c_p in the argument of the error function in Equation 2.2.19 would lie in the range of $0.55 < c_{p,\ app} < 0.70$ to compensate for the phase change effect in the exact solution based on the $c_p = 0.32$. The value of $c_{p,\ app}$ is somewhat higher than that obtained from Equation 2.2.25. The difference can be explained by the influence of the latent heat on the temperature gradient (Equation 2.2.14) and, by the fact that the storage material does not actually attain temperature t_a, but a temperature $t > t_a$. For our discussion in Section 2.2.3, we will use a $c_{p,\ app} = 0.60$ Btu/lb-°F.

2.2.2. Heat-Exchanger Design Parameters for a PCM System

2.2.2.1. Relationship Between Thermal Efficiency, Period and Depth of Storage Unit

Relationships between these variables for a regenerative heat transfer system can be obtained using a global analysis without special reference to the internal temperature profile. Consider the schematic in Figure 2.2.4, showing a regenerative system wherein the working fluids enter the system with a square-wave temperature variation A. Responding to this driving function, the heat storage material exhibits behavior B and, in turn, converts the fluids output function to C. The cross-hatched areas in C denote the energy usefully transferred from one fluid to the other. This energy is to be maximized subject to the operational, physical, and economical constraints imposed on the system. Thermal response of the heat storage material is given as [5]

$$\frac{di}{d\tau} = UA\ (t - t_a) \qquad (2.2.27)$$

where $i = c_p mt$ is the total enthalpy of the heat storage mass m so that Equation 2.2.27 can be written as $\frac{dt}{d\tau} = \frac{UA}{c_p m}(t - t_a)$,

and on integrating,

$$\ln(t - t_a)\Big|_{t_{\text{initial}}}^{t_{\text{final}}} = \left[\frac{UA\,\tau}{c_p\, m}\right] \qquad (2.2.28)$$

The nondimensional group $\left[\frac{UA\tau}{c_p\, m}\right]$ is known in the regenerator design practice as the "reduced time," and is often given with both the heat transfer area, A, and the regenerator mass, m, calculated on the basis of 1 unit of free volume:

$$\frac{UA\tau}{c_p m} = \frac{U(A/V)\tau}{c_p\,(m/V)} = \frac{UA'''\tau}{c_p\, m'''} \equiv \Pi \qquad (2.2.29)$$

Note that $m/V \equiv m'''$ with the dimensions of mass / volume is not the true density of the material, ρ, but is the mass of the storage material in any arbitrary configuration per unit volume of the device.

Similarly the working fluid Equation 2.2.5 becomes

$$v\,\frac{dt_f}{dz} = -\frac{U(A/V)}{c_{pf}\,\rho_f}(t_f - t)$$

$$\frac{dt_f}{t_f - t} = -\frac{U(A/V)}{c_{pf}\,\rho_f\, v}\, dz \qquad (2.2.30)$$

$$\ln(t_f - t)\Big|_{t_{f,\text{in}}}^{t_{f,\text{out}}} = -\left[\frac{U(A/V)}{c_{pf}\, G}\right] z \qquad (2.2.31)$$

where the group $\left[\frac{U(A/V)\,Z}{c_{pf}\, G}\right]$ is known as the "reduced length" of a regenerator, Λ, and G is mass velocity. The ratio $\Pi/\Lambda \equiv u$, the utilization factor, can be viewed as the ratio of the heat capacity of the fluid to that of the matrix, or a measure of the degree to which the storage material is being utilized.

The thermal recovery, η, is defined as the ratio of heat actually recovered to the maximum recoverable heat. Thus –

$$\eta = \frac{\bar{t}_{\text{outlet (cold stream)}} - t_{\text{inlet (cold stream)}}}{t_{\text{inlet (hot stream)}} - t_{\text{inlet (cold stream)}}} \qquad (2.2.32)$$

The results are available in the form shown on Figure 2.2.5.

From these curves the designer may select Λ and Π for any thermal recovery η, thereby fixing his design point. In using Figure 2.2.5 for a rough assessment of the system parameters, the following points should be kept in mind:

1. For a given $\Lambda = \frac{U(A/V)z}{c_{pf}\,G}$, the highest recovery is obtained with the lowest $u = \Pi / \Lambda$. This means that for a given G either the halfcycle τ should be short or the mass of storage matrix should be very large. τ is fixed for a daily storage cycle and an excessively large matrix mass is costly and undesirable.

2. Recovery improves with the greater Λ values, but again, for a given G, this means either a larger z (a greater unit length, i.e., size) or higher heat transfer coefficients h (at the expense of the pumping energy) are required. A compromise here is unavoidable.

3. The half periods are not expected to be equal, but assuming that the sum of reduced times is kept constant, $\Pi_1 + \Pi_2$ = constant, and only the ratio Π_1 / Π_2 is allowed to vary, Figure 2.2.5 can still be used to compute the thermal recovery. Saunders and Smoleniec recommend the following method: For a given utilization factor, u, calculate the recovery η assuming both Π's at the first half-cycle value, then cauculate an η with both Π's at the second half-cycle value; take the arithmetic mean of the two values.[5] Note that since the u-curves are all convex upward, the mean is always less than the value which would be obtained if Π_1 and Π_2 were equal. This means that equal Π's offer the best recovery ratio.

2.2.2.2. Temperature Response of a Storage Unit

To estimate the temperature response of a storage unit undergoing cyclic operation, we have used the periodic solution of Equation 2.2.21. The following values are calculated for our storage system –

- $c_{p,\,app}$ = 0.60 Btu/lb-°F (assumed; based on discussion in Section 2.2.1.2.2)
- τ_o = total period = 24 hours for a daily cycle

- $\alpha_{app} = 0.0153$ sq ft/hr
- $K = 3\ \mathrm{ft}^{-1}$
- $\lambda = 2.1$ ft
- Phase Velocity $= \lambda \nu = \frac{2.1}{24} = 0.0875$ ft/hr $= 1$ in./hr

This means that as a first approximation, in terms of orders of magnitude only, the designer of a periodic energy storage system (daily cycle) utilizing $LiKCO_3$ as a storage material and operating between the melting point (505°C) and ambient temperature at (22°C) should think in terms of 2-foot long temperature waves penetrating the material with the speed of about 1 in./hr. Note, however, that in the case of any harmonic oscillation (e.g., a sine-wave input), the amplitude of the incoming wave will be damped by $\exp(-2\pi) = 0.0019$ over a single wave length. With such damping, choosing the thickness of the material on the order of a whole wavelength would appear to represent underutilization and therefore waste. Thus, we would like to determine an optimum thickness or distance between the heat exchange surfaces.

In working with a slab of finite thickness 2a, it is convenient to define a dimensionless frequency M,

$$M = \sqrt{\frac{\pi a^2}{\alpha \tau_o}} \tag{2.2.33}$$

M can also be expressed in terms of a Fourier number based on the slab half thickness, a, and the total period τ_o:

$$\overset{\circ}{N}_{Fo} = \frac{\alpha \tau_o}{a^2} \tag{2.2.34}$$

So $$M = \sqrt{\frac{\pi}{\overset{\circ}{N}_{Fo}}} \tag{2.2.35}$$

The temperature response of a slab to a cyclic heat input is usually expressed in terms of the parameter M. The relevant solutions are available in literature but their numerical evaluation is laborious.[4,6]

Results that may have a bearing on the design of a TES system are shown graphically in Figures 2.2.6 and 2.2.7.

Figure 2.2.6 shows how the temperature amplitude θ falls off as the wave penetrates the slab. θ "swings" between the values of -1 and $+1$ under an input of the form $\cos \omega t$ but only the positive half is plotted as a fraction of the impressed amplitude. The true temperature, t, is obtained from the relationship

$$\theta = \frac{2t - t_{max} - t_{min}}{t_{max} - t_{min}} \qquad (2.2.36)$$

Thus if the hot fluid enters the system at t_{max} = 650°C (1200°F) and the cold fluid is at t_{min} =360°C (682°F), then halfway between the surface and the center of the slab (relative depth =0.5) a) θ =0.2 and t =535°C, if the heat transfer coefficient at the surface is infinite; and b) θ = 0.12, t =522°C, if the Biot number equals 5. It is of interest that the surface amplitude is only 60% of the ambient amplitude even at the relatively high surface heat transfer indicated by the N_{Bi} = 5. Knowing that the surface will not exceed a certain temperature limit, even though one of the "working" fluids is considerably hotter, may help in the choice of the storage material.

The variation of θ at the slab core with frequency M, for a constant ratio of the surface-to-interior conductances U/k_s =5 ft^{-1} is shown on Figure 2.2.7. With the period fixed at 24 hours, this can be viewed as a variation of θ with slab thickness. Note, however, that although the surface amplitude fraction θ is independent of the slab thickness; it does depend on the period τ according to the relationship

$$\theta = \frac{1}{\sqrt{1 + 2p + 2p^2}} \qquad (2.2.37)$$

where $p = \dfrac{M}{N_{Bi}} = \dfrac{k_s}{U} \sqrt{\dfrac{\pi}{\alpha_s \tau_o}}$

Unfortunately, in dealing with daily storage the duration of the period, τ_o, is not a free design parameter.

2.2.2.3. Amount of Energy Stored

A measure of the heat storage capacity of a cyclic storage device can be obtained by integrating the temperature wave over a half cycle temperature wave. (In cyclic operation, the energy stored during the first half cycle equals the amount retrieved during the second half cycle, their algebraic sum being zero). Referring the integral of the wave form, i.e., the storage capacity, to the heat content of the material at the maximum temperature that could be attained by the surface or the ambient yields the fraction of the energy stored or an "effectiveness" of the storage matrix. This is shown in Figure 2.2.8, where the fraction stored is plotted as a function of the frequency M for sine-wave and square-wave profiles. Predictably, the square-wave variation of the energy input utilized the storage volume better than the sine-wave variation.

Figure 2.2.9 shows the fraction of the maximum possible energy stored in a circular, cylindrical rod as the ambient temperature varies harmonically and the heat transfer at the surface is measured by a finite heat transfer coefficient U (Btu/hr-sq ft-°F). The introduction of this heat transfer coefficient results in a family of curves parameterized by the nondimensional group $N^2_{Bi} \; \overset{\circ}{N}_{Fo} = \frac{U^2 \alpha \tau_o}{k^2}$, which does not depend on the cylinder radius. For a fixed period τ_o, Figure 2.2.9 gives the effectiveness of this configuration (circular rods submerged in the working fluids) as a function of size for varying intensities of heat transfer at the surface.

In a special case, the capability of a slab to store energy has an optimum. The physical interpretation here is that while very little heat can be stored in a thin slab (small "a" or M for a fixed period τ_o), a semi-infinite body with its surface temperature varying harmonically can store, at the most, $\sqrt{2/\pi}$ or 0.798 of the maximum. Groeber[7] observed that the heat stored during a half cycle can be expressed by

$$Q_{0.5\,cy} = 2A\sqrt{kc_p \rho \tau_o} \;\; \Delta t_{0.5} \cdot \;\; \Phi(M) \qquad (2.2.38)$$

where

A = slab surface area

$\Phi(M)$ = frequency-dependent function,

$$\Phi(M) = \sqrt{(\pi/2)\ \ (\cosh^2 M - \cos^2 M / (\cosh^2 M - \sin^2 M)}$$

$\Delta t_{0.5}$ = half the impressed amplitude (°F above the mean temperature)

The frequency-dependent function $\Phi(M)$ goes through a maximum of 0.911 at $M = 1.2$, and decreases for $M > 1.2$ until the limit of 0.798 is reached for practically all $M > 3$. (See Figure 2.2.10.)

This suggests that, in the absence of other overriding considerations, the designer of a storage device with a flat plate matrix might start at $M = 1.2$. Experience shows, however, that tradeoffs between competing effects such as those mentioned in the discussion of Figure 2.2.5 are often unavoidable.

2.2.3. Experimental Verification of Simplifying Assumptions

A pilot model 5-in. tall, 3-in. diameter, with a 1/2-in. OD interior well, was used to study solidification half cycles with the model salt. For exact dimensions, construction details, and the other thermocouple placement, see Figures 2.4.3 and 2.4.4. This study confirmed two assumptions developed and used in the analytical treatment of the heat storage problem with a phase change: 1) assume that there is no thermal gradient in the liquid phase, so that in a cyclic operation the solidification half cycle always begins with a uniform temperature distribution, permitting the use of transient ("single blow") solutions; 2) use an "apparent" c_p for system design. Both assumptions appear to be confirmed by the test results also shown on Figure 2.2.11.

2.2.3.1. The No-Thermal-Gradient Assumption: First Part of the Cooling Half Cycle (Cooling the Liquid)

The model system ($LiKCO_3$) was heated to about 50°C above the melting point (500°C). Cooling begins with the liquid phase uniformly at 550°C. The cooling was provided by 22°C air passing through the 0.43-inch ID internal well at 50 ft/s. Using the Dittus-Boelter equation[8] for turbulent forced convection inside tubes in the form

$$h = 0.020\ (125)\ G^{0.8}\ (0.43/12)^{-0.2} \qquad (2.2.39)$$

where G is the mass velocity, $G = \rho v = 0.0742\ (50) = 3.71\ lb_m/sq\ ft\text{-}s$, and constant 125 is a temperature-dependent factor involving air conductivity and viscosity ($k/\mu^{0.8}$). The heat transfer coefficient is calculated as 13.9 Btu/hr-sq ft-°F. Several trial-and-error calculations of the exit air temperatures based on the relationship between the increase of the enthalpy of air and the heat transferred from the hot charge along the interior well length z,

$$c_p \dot{m} \frac{dt}{dz} = hp\ (\bar{t}_w - t)$$

or, integrated

$$\frac{t_{exit} - t_w}{t_a - t_w} = \exp\left[-\frac{hp\ z}{c_p \dot{m}}\right] \qquad (2.2.40)$$

where

c_p = specific heat of air = 0.25 Btu/lb$_m$ - °F

$\dot{m}$ = air mass flow-rate, 13.5 lb$_m$/hr

p = inner well perimeter = $\pi(0.43/12)$, ft

z = total path traveled by air (5-in.)

t_a = inlet air temperature

$\bar{t}_w$ = mean wall temperature ≈ 977°F = 525°C

lead to a corrected heat transfer coefficient value of h = 13 and the bulk air temperature of 65.6°C (150°F) ≡ $\bar{t}_{air}$. The knowledge of $\bar{t}_{air}$ and of the surface coefficient, h, allows us to calculate the temperature in the liquid phase using standard solutions for conduction heat transfer with the boundary conditions of the third kind. Using a solution[9] for hollow cylinders which assumes a finite conductivity of the material (i. e., no mixing) yields curves

(A_1 and B_1, Figure 2.2.11), failing to reproduce the experimental results (curves A, B).

The assumption of perfect internal mixing and no temperature gradient leads to a cooling rate of

$$-\frac{dt}{d\tau} = -\frac{hpz\,(\bar{t}-150)}{60\,c_p\,m} \cong -8\ {}^\circ\mathrm{F/min}\ (\cong\ 5^\circ\mathrm{C/min})$$

which reproduces the experimental cooling rate of about 5°C/min, and, on integrating to $t = 150 + 872 \exp(-0.0116\,\tau)$, where τ is in minutes, matches the experimental time-temperature curves A and B quite accurately. This suggests vigorous convective (bouyancy driven) mixing in the liquid phase in a cell of the size used here.

In fact, with the kinematic viscosity of the liquid estimated at $\nu = 0.17$ sq ft/hr and the thermal diffusivity $\alpha_\ell = 0.0183$ sq ft/hr, the Prandtl number $\nu/\alpha \cong 9$ (comparable to that of water at room temperature), the coefficient of volume expansion ,

$$\beta = \frac{\rho_\infty - \rho}{\rho\,\Delta t} \cong 1.4 \times 10^{-4}\ {}^\circ\mathrm{R}^{-1}\ ,\quad \Delta t \sim 50^\circ\mathrm{C}\ (=90^\circ\mathrm{F}),\ \text{the}$$

significant dimension being $L \cong 1/12$, the Rayleigh number is of the order of 10^6. This is several orders of magntidue higher than the stability criterion of the order $N_{Ra} = 10^3$.[10] The Rayleigh number $N_{Ra} = \frac{g\,\beta\,\Delta T L^3}{\alpha\,\nu}$ measures the ratio of buoyant to thermal forces in a fluid.

To approach the condition of stability, the width of the liquid-filled gap would have to be reduced by a factor of ten, to about 1/10 of an inch. Subsequent experiments on solidifying the model storage system ($LiKCO_3$) in a honeycomb matrix of about 1/4 inch mesh showed some temperature gradient between thermocouples A and B but not to the extent predicted by the noconvection solution curves A_1 and B_1.

2.2.3.2. Use of an "Apparent" c_p: Second Part of the Cooling Half Cycle (The Phase Change)

Figure 2.2.11 shows a brief (about 2.5-minute) isothermal time lag at 500°C for Thermocouple A and a 22-minute time lag for Thermocouple B. Megerlin's solution (Equation 2.2.13, Figure 2.2.3) for $N_{ph} = 0.48$ and $N_{Bi} = 0.2$ predicts longer solidification times, 4.7 and 28 minutes, respectively. This solution, however, is written for an infinitely long cylinder with the heat sink at the interior well only. When heat losses from the outer lateral surface and from the top and bottom are added to the central well loss and the cooling rates are recalculated on that basis, the isothermal lag times becomes 2.7 minutes for thermocouple A and 20 minutes for thermocouple B.

2.2.3.3. Third Part of the Cooling Half Cycle: Cooling the Solid Phase

Thermocouple A is embedded into a solid beginning at 12.5 minutes (Figure 2.2.11). The apparent c_p over a temperature range of 505° to 445°C (941° to 833°F) is $0.32 + 148/108 = 1.69$. Used in the analytical solution for the hollow cylinder, it results in the curve A_2, closely following the experimental curve A over this range. (The use of $c_p = 0.32$, i.e., of the sensible heat alone, results in Curve A_2'), which does not agree with the experimental data).

Thermocouple B is so close to the outer wall that by the time its position has changed from the liquid to the solid phase the whole mass is solid; there is no evolution of the latent heat, and $c_{ps} = 0.32$ used in the analytical solution adequately describes the behavior of thermocouple B (curve branch B_2, Figure 2.2.11).

2.2.4. Design of Experimental Storage Unit

Based on the considerations discussed in the previous sections, particularly the results of Bramlette et al., discussed in Section 2.2.1., and the experimental results from the pilot unit, we have selected an annular arrangement for the experimental storage unit. This arrangement can be scaled-up; in a commercial-size unit a multi-unit hexagonal cell arrangement may be visualized. Also this arrangement is the simplest experimentally. The heat input will be provided by an electrical heater and the heat output will be provided by air. Detailed design of the unit will be discussed in a separate task report, and only the selection of suitable dimensions and insulation is presented here.

The interior radius $r_o = 1$ inch was chosen so that the well would be large enough to hold electric heating elements yet small enough to generate a fully developed turbulent flow of the coolant.

The corresponding Reynolds number for air, with $d = 2r_o = 1/6$ ft, $N_{Re} = \frac{vd}{\nu} = 10^5 v/(6)(16) \cong 10^3$ v. An air velocity of 10 ft/s would result in 10,000, turbulent flow, a Nusselt number of $N_{Nu} = 0.020\ N_{Re}{}^{0.8} = 31.7$ and a heat transfer coefficient of $h = (31.7)(6)(0.115) \cong 3$ Btu/hr sq ft-^{0}F. The resulting Biot number, $N_{Bi} = \frac{hr_0}{k} = \frac{3}{12(1.3)} \cong 0.2$. Similarly, a 50 ft/s air velocity will produce a Biot number of about 0.6.

Using a 12-hour half-period and the properties of the model system ($LiKCO_3$) results in a Fourier number ($N_{Fo} = \frac{\alpha \tau}{r_o{}^2} = \frac{0.0287(12)}{(1/12)^2}$) of about 50. Using Figure 2.2.3. ($N_{ph} = 0.57$) with $N_{Fo} = 50$ and a range of N_{Bi} from 0.2 to 0.6, we see that an $R = \frac{r}{r_0}$ of 5 to 6.5 or an external radius of 5 to 6 inches, can be expected.

Assuming a 6-inch outside radius, 1 cubic foot of the reference salt would fill the cylinder to 1.3 feet in height.

The insulation was selected from the following considerations - under steady-state conditions the temperature distribution in a cylinder is given by

$$\frac{d}{dr}\left(r \frac{dt}{dr}\right) = 0 \qquad (2.2.41)$$

Integrating twice and using the condition at the insulation boundary

$$-k \frac{dt}{dr} = h_2(t_2 - t_a) \tag{2.2.42}$$

leads to

$$\frac{t_1 - t_2}{t_2 - t_a} = \frac{h_2 r_2}{k_{ins}} \ell n \frac{r_2}{r_1} \tag{2.2.43}$$

where the subscripts denote:

1 = outside radius, storage unit
2 = outside radius, insulation
a = ambient
ins. = insulation

If it is desired, for safety reasons, and to keep heat losses low, to keep the outside insulation face at 54°C (130°F) or below, then t_1 = 505°C (941°F) t_2 = 54°C(130°F), t_a = 22°C(72°F), h = 1.5 Btu/hr-sq ft-°F (combined radiation and free convection), and k_{ins} = 0.05 (mineral wool) lead to a r_2 of about 10 inches, or an insulation layer 10 − 6 = 4 inches thick. A comparable thickness of insulation should also be used on the top and bottom insofar as is practicable.

To recapitulate, 1 cubic foot of the reference TES material can be cooled from the melting temperatures to a complete solidification in about 12 hours in a hollow cylindrical container 1 foot in diameter and 1.5 feet tall with a 2-inch interior well diameter through which room-temperature air is passed at about 50 ft/s.

With a 4-inch thick insulation, starting at a uniform 22°C (72°F) temperature, an electric power input equal to

$$\frac{1}{3413}\left[\frac{141.5(0.32)(941-72)+141.5(148)}{12}+1.5(6.76)(130-72)\right] \cong 1.64 \text{ kW}$$

would be required, at the most, to melt the charge in the 12-hour half cycle. This amounts to an energy flux at the interior wall of

$$\frac{1.64 \times 3413}{0.785} = 7130 \frac{\text{Btu}}{\text{hr-sq ft}}$$

Based on the above calculations, the Engineering Scale TES System has been designed and constructed for the evaluation of its operating performance.

2.2.5. Computer Modeling of the Performance of the Experimental Storage Unit

In Sections 2.2.2. through 2.2.4, we utilized various approximations to elucidate relationships among various system design parameters. These approximations, however, cannot properly simulate an operating storage unit, because the available solutions do not account for:

1. Finite length of the storage unit
2. Heat losses at the outer walls and at the bottom and top of the unit.
3. Variation in cooling air temperature in the z direction. Thus the solid/liquid interface does not lie in a cylindrical plane parallel to the cooling surface.

It is possible to incorporate these conditions in a finite difference scheme and computer solution. The finite difference mesh can be refined sufficiently to avoid truncation and round-off errors, although some uncertainty in the results, due primarily to our imperfect knowledge of the property values and to the system's interaction with the ambient conditions, will remain. The latter problem (external heat transfer coefficients, parasitic heat losses, etc.) will be formulated using currently accepted correlations. It is expected that the data obtained experimentally will have a comparable accuracy so that parallel experimental/mathematical model runs can be used to precisely define the essential parameters of this thermal energy storage system.

Unlike Equations 2.2.1 and 2.2.2, the heat balance on a volume V with a heat transfer surface A is written in terms of specific enthalpy i, Btu/lb_m:

$$\frac{\partial}{\partial \tau} \int_V \rho \, i dV = \int \int_A k \text{ grad } t \cdot d\vec{A} \qquad (2.2.44)$$

Applying the Green-Gauss theorem to the right hand side of Equation 2.2.44,

$$\iint_A k \operatorname{grad} t \cdot d\vec{A} = \int_V k \operatorname{div} \operatorname{grad} t \, dV$$

and expressing it in axisymmetric cylindrical coordinates (r, z) yields

$$\rho \frac{\partial i}{\partial \tau} = k\left(\frac{\partial^2 t}{\partial r^2} + \frac{1}{r}\frac{\partial t}{\partial r} + \frac{\partial^2 t}{\partial z^2}\right) \qquad (2.2.45)$$

Temperature t is a piecewise continuous function of the enthalpy i such that

$$i = c_{ps} t, \quad t < t_m \qquad (2.2.46a)$$

$$c_{ps} t_m \leq i \leq c_{p\ell} t_m + \Delta H_f, \quad t = t_m \qquad (2.2.46b)$$

$$i \geq c_{p\ell} t_m + \Delta H_f, \quad t = \frac{i - \Delta H_f}{c_{p\ell}} \qquad (2.2.46c)$$

Initially, at $\tau = 0$, the temperature distribution is an arbitrary function of position,

$$t = t(r, z, o) \qquad (2.2.47)$$

Boundary conditions on A are of the third kind

$$-k \operatorname{grad} t = U(t_a - t) \qquad (2.2.48)$$

or of the second kind

$$-k \operatorname{grad} t = \dot{q}'' \qquad (2.2.49)$$

where $\dot{q}''\left[\frac{\text{Btu}}{\text{hr-sq ft}}\right]$ is the prescribed flux at portions of the surface A, or the combination of both kinds of boundary conditions.

If it is found experimentally that a TES material exhibits a solid-liquid transition over a measurably wide temperature range, $t_m - \epsilon$, $t_m + \epsilon$, Equation 2.2.46a, b and c can be written as

$$i = c_{ps}t, \; t<t_m \qquad (2.2.46d)$$

$$i = i(t_m - \epsilon) + \frac{\Delta H_f}{2\epsilon}(t - t_m + \epsilon), \; t_m - \epsilon \leq t \leq t_m + \epsilon \qquad (2.2.46e)$$

$$i = i(t_m + \epsilon) + c_{p\ell}(t - t_m - \epsilon), \; t \geq t_m + \epsilon \qquad (2.2.46f)$$

Schematically, the specific enthalpy will follow the curve of Figure 2.2.12.

Formulation of Equations 2.2.44 through 2.2.49 in terms of an explicit differencing scheme results in a straightforward numerical procedure. The underlying mathematical concept of "weak" solutions and proof of convergence of the differencing scheme chosen here is discussed by Atthey.[10]

An explicit differencing scheme written for the axisymmetric of Figure 2.2.13 requires 9 kinds of nodal equations: 4 edge points, 4 surface points of a general interior point (i,j) for the cooling half cycle. Two edge points and the interior surface are modified for the melting half-cycle to reflect the boundary condition of the second kind (Equation 2.2.49).

Thermal behavior of the working fluids passing through the central cooling tube follows from the heat balance on the fluid as it exchanges energy with the interior wall of the unit. Analogously to Equation 2.2.5, we have

$$-\frac{Di_f}{D\tau} = UA\,(t_f - t_{surf}) \qquad (2.2.50)$$

enthalpy $\left[{\text{loss} \atop \text{gain}}\right]$ by the working fluid = energy transferred $\left[{\text{to} \atop \text{from}}\right]$ the storage material, or in the z-direction with j = 0, 1, 2 .... p, p + 1.

$$t_{fo} = t_{f,\,initial}\text{, an input variable} \qquad (2.2.51a)$$

$$t_{fi} = t_{fo} - \frac{\mathfrak{C}}{2}\left(t_{fo} - \frac{t_{11} + t_{12}}{2}\right) \qquad (2.2.51b)$$

$$t_{fj+1} = t_{fi} - \mathfrak{C}\left(t_{fj} - \frac{t_{1,j} + t_{1,j+1}}{2}\right), \; j = 1,2, \ldots p \qquad (2.2.51c)$$

$$t_{fp+1} = t_{fp} - \frac{\mathfrak{C}}{2}\left(t_{fp} - \frac{t_{1,p} + t_{1,p+1}}{2}\right) \qquad (2.2.51d)$$

where $\mathfrak{C} = \dfrac{\pi\, dh\, \delta z}{\dot{m}\, c_{pf}}$

δz = vertical subdivision, $p \cdot \delta z$ = height of unit, z
d = diameter, central cooling tube
h = heat transfer coefficient, fluid to inner wall surface
$\dot{m}$ = mass flow rate of fluid, lb_m/hr
c_{pf}= = average specific heat of working fluid

During the heating cycle the electric input is specified directly in

$$\dot{q}'' \left[\frac{\text{Btu}}{\text{hr-sq ft}}\right] \text{or } \dot{q}''. \pi d \delta z$$

for each vertical subdivision.

The finite difference formulation, with detailed nodal equations, the solution algorithm and the stability criteria precede the program listing in Fortran IV.

2.2.6. Conclusions of Section 2.2.

Problems arising in the design of a heat-storage-and-retrieval device operating on both sides of the phase change discontinuity have been attacked by a system-analytical approach using the "apparent c_p" parameter. This parameter includes both the latent heat of fusion and the perturbation in the temperature gradient to the standard solutions describing the operation of regenerative heat storage devices and offers a set of first estimates in the design of a TES system with phase change.

Our experimental observation from the pilot TES runs that the liquid phase of the heat storage material has no appreciable temperature gradient permitted the use of a highly accurate solution in a realistic geometry: that of a hollow cylinder alternately heated and cooled from its internal well. The solution was used to provide design data for the laboratory-scale TES model currently under construction. Formulated in terms of dimensionless parameters, the solution may be used for a variety of other materials, cycle times, and TES systems sizes.

The experimental work on the pilot TES model provided justification for the use of simplifying assumptions inherent in the methods discussed above and verified the correlations used in calculating its heat transfer and time-temperature relationships. It also provided useful inputs into the construction of the more general TES model written in terms of finite differences and intended for computer simulation of the performance of the engineering-scale model.

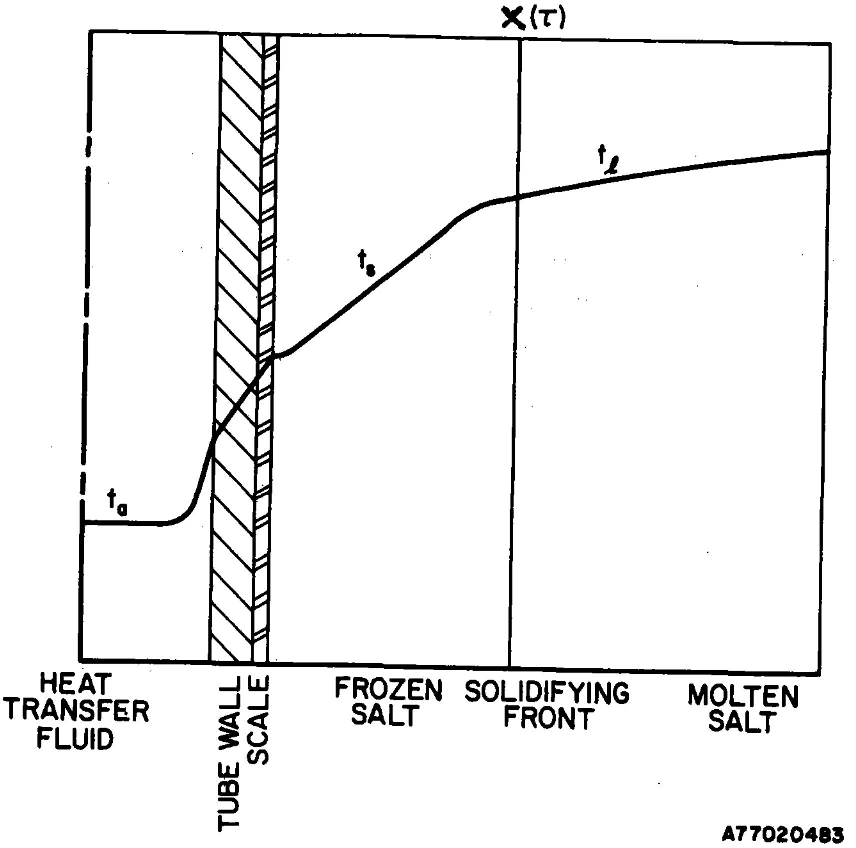

Figure 2. 2. 1. SCHEMATIC OF TEMPERATURE PROFILE IN A PHASE-CHANGE THERMAL ENERGY STORAGE UNIT

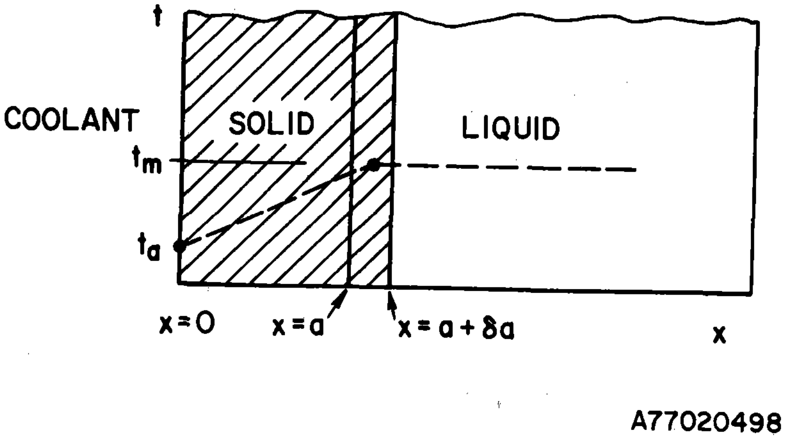

Figure 2. 2. 2. ADVANCE OF THE FREEZING FRONT AT x = a

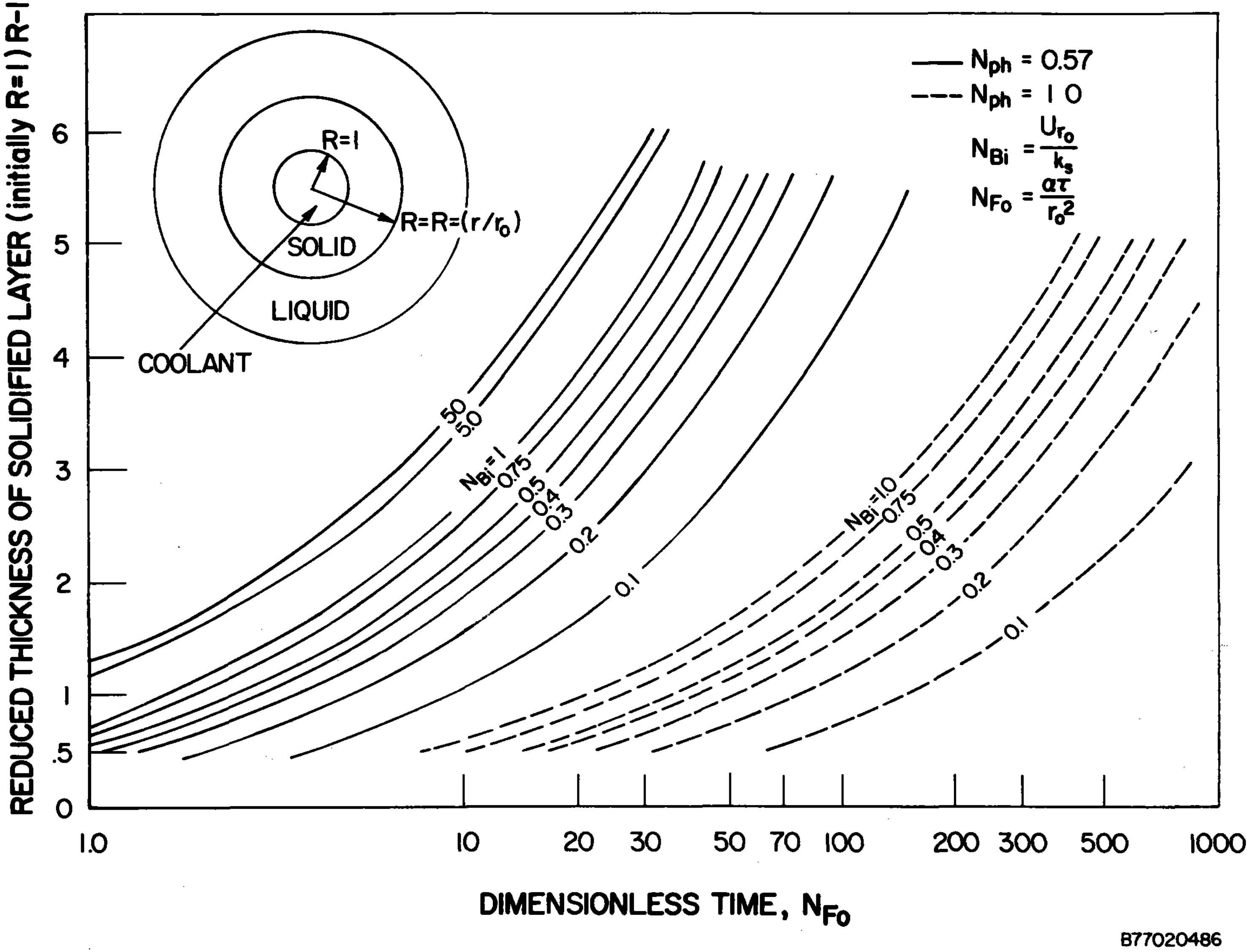

Figure 2.2.3. SOLIDIFICATION OF A CYLINDRICAL MELT FROM WITHIN

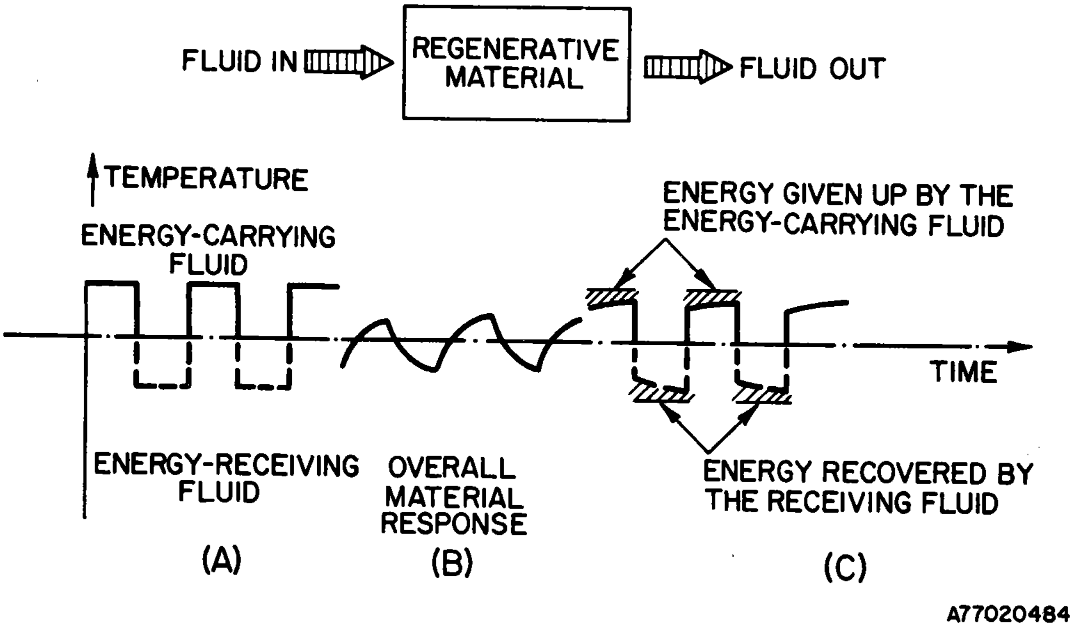

Figure 2.2.4. CYCLIC OPERATION OF A HEAT STORAGE-AND-RETRIEVAL DEVICE

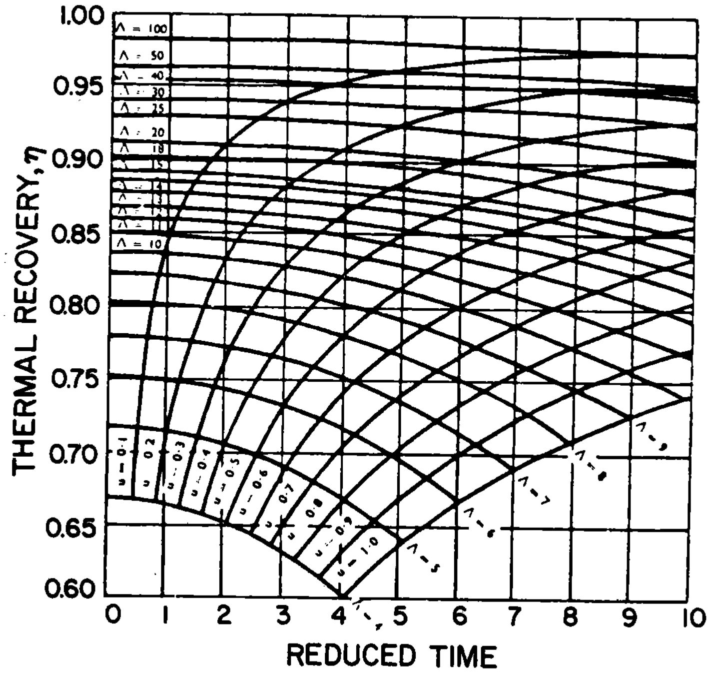

A77020485

Figure 2.2.5. COMPUTED THERMAL RECOVERY FOR A RANGE OF REDUCED LENGTHS (4 to 100) AND A RANGE OF REDUCED TIMES (0-10) (u = UTILIZATION FACTOR, Π = REDUCED TIME OF PERIOD, η = THERMAL RECOVERY, Δ= REDUCED LENGTH OF REGENERATOR)[5]

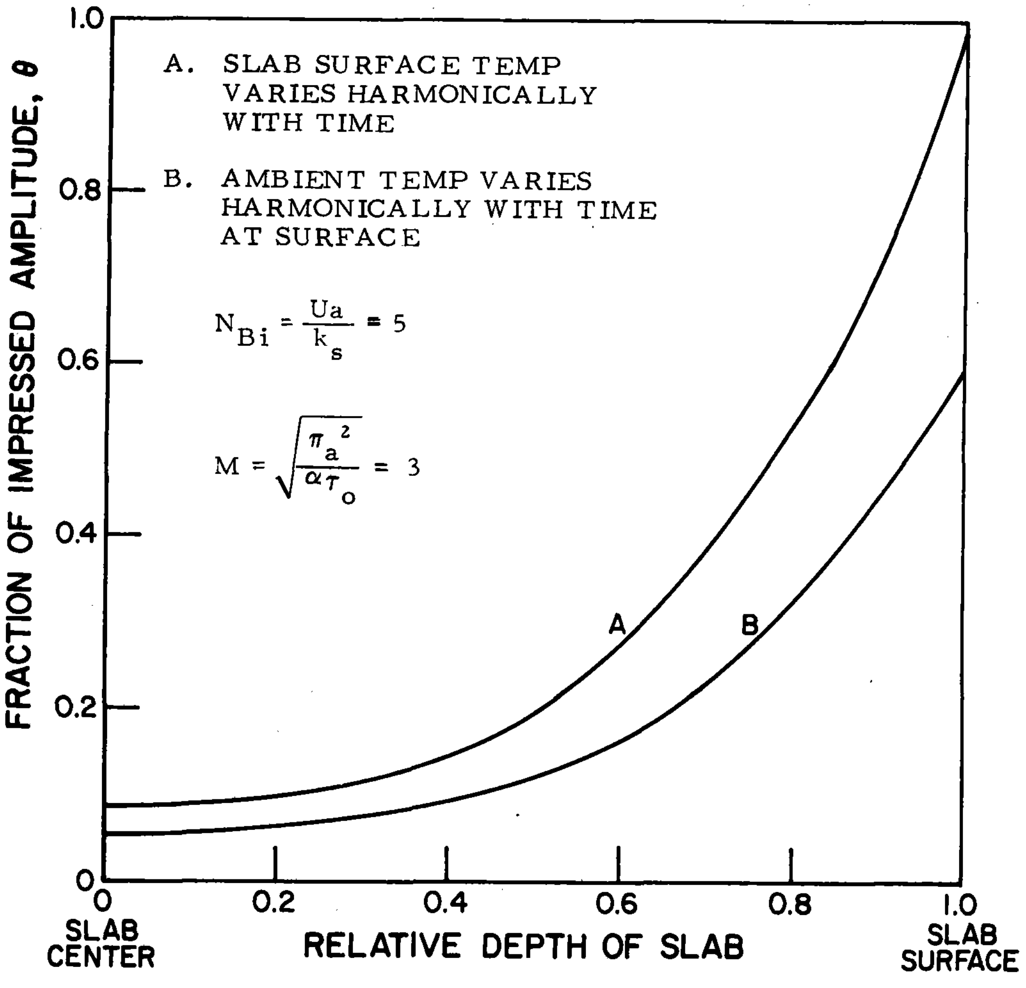

A77020490

Figure 2.2.6. AMPLITUDE OF A TEMPERATURE WAVE PENETRATING A SLAB FROM BOTH FACES

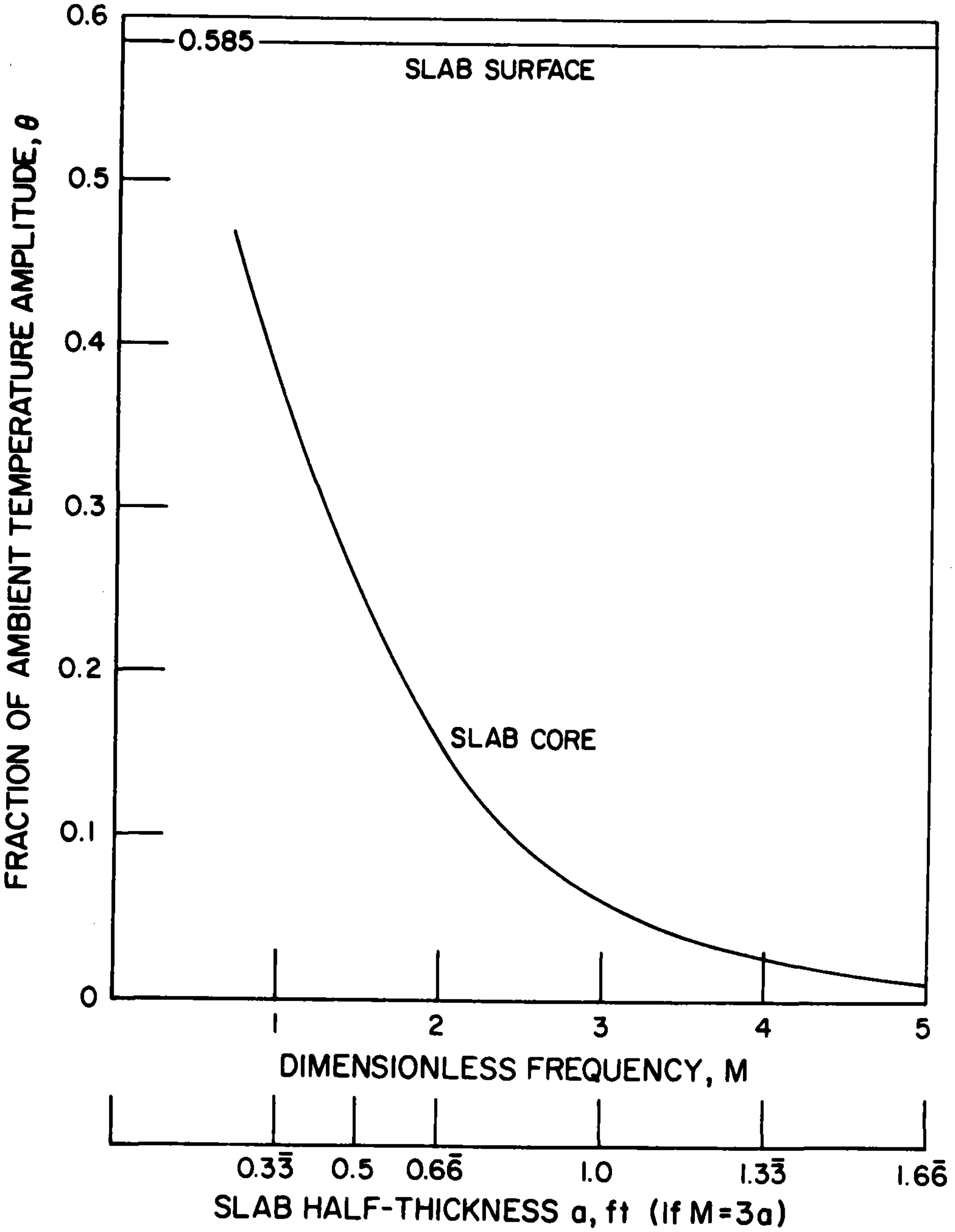

A77020491

Figure 2.2.7. FRACTIONAL TEMPERATURE AMPLITUDE AT THE CENTER AND THE SURFACE OF A SLAB SUBJECTED TO A HARMONICALLY VARYING AMBIENT WITH U/k = 5 ft^{-1}

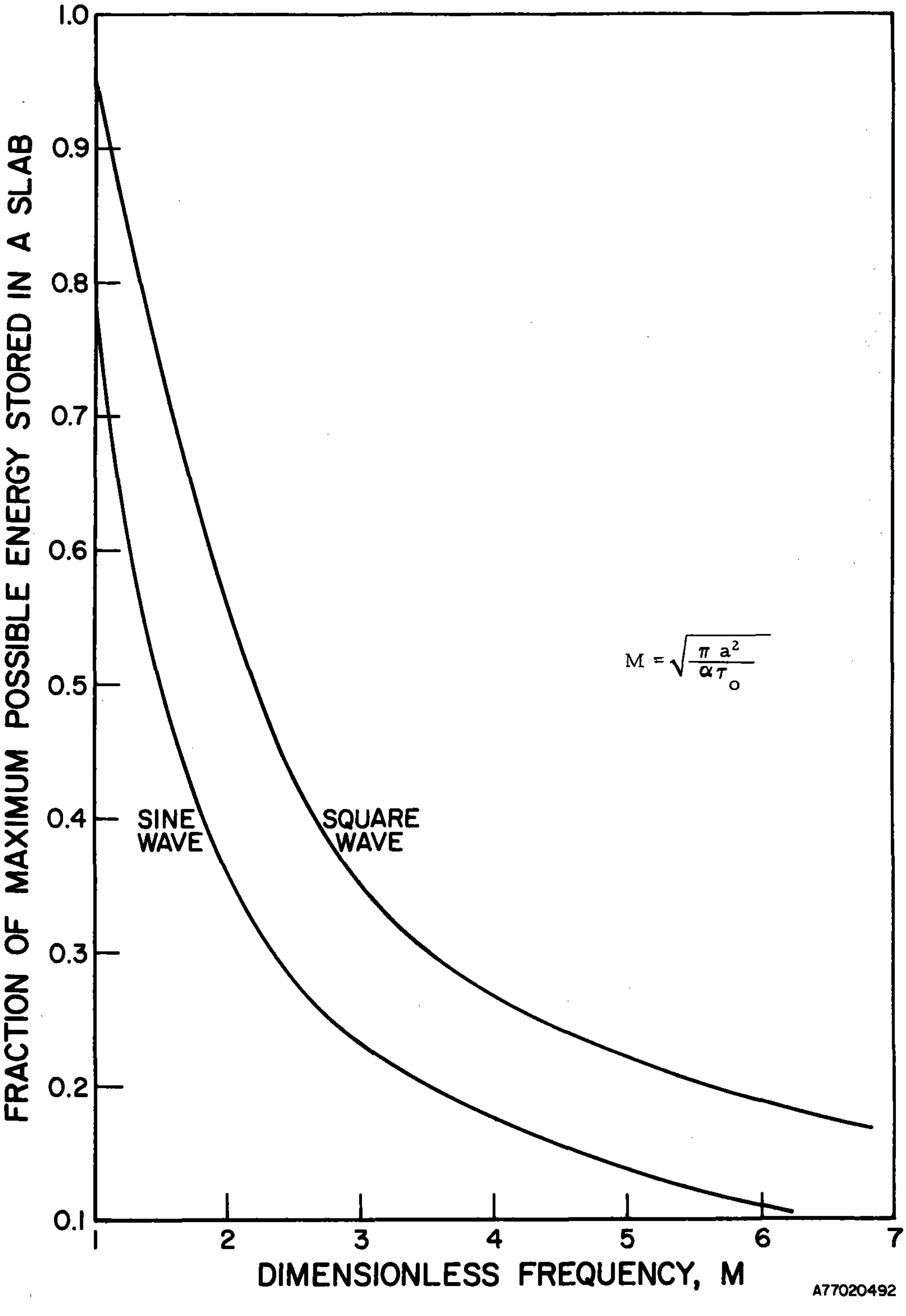

Figure 2.2.8. ENERGY STORAGE IN A SLAB WITH PERIODICALLY VARYING SURFACE TEMPERATURES

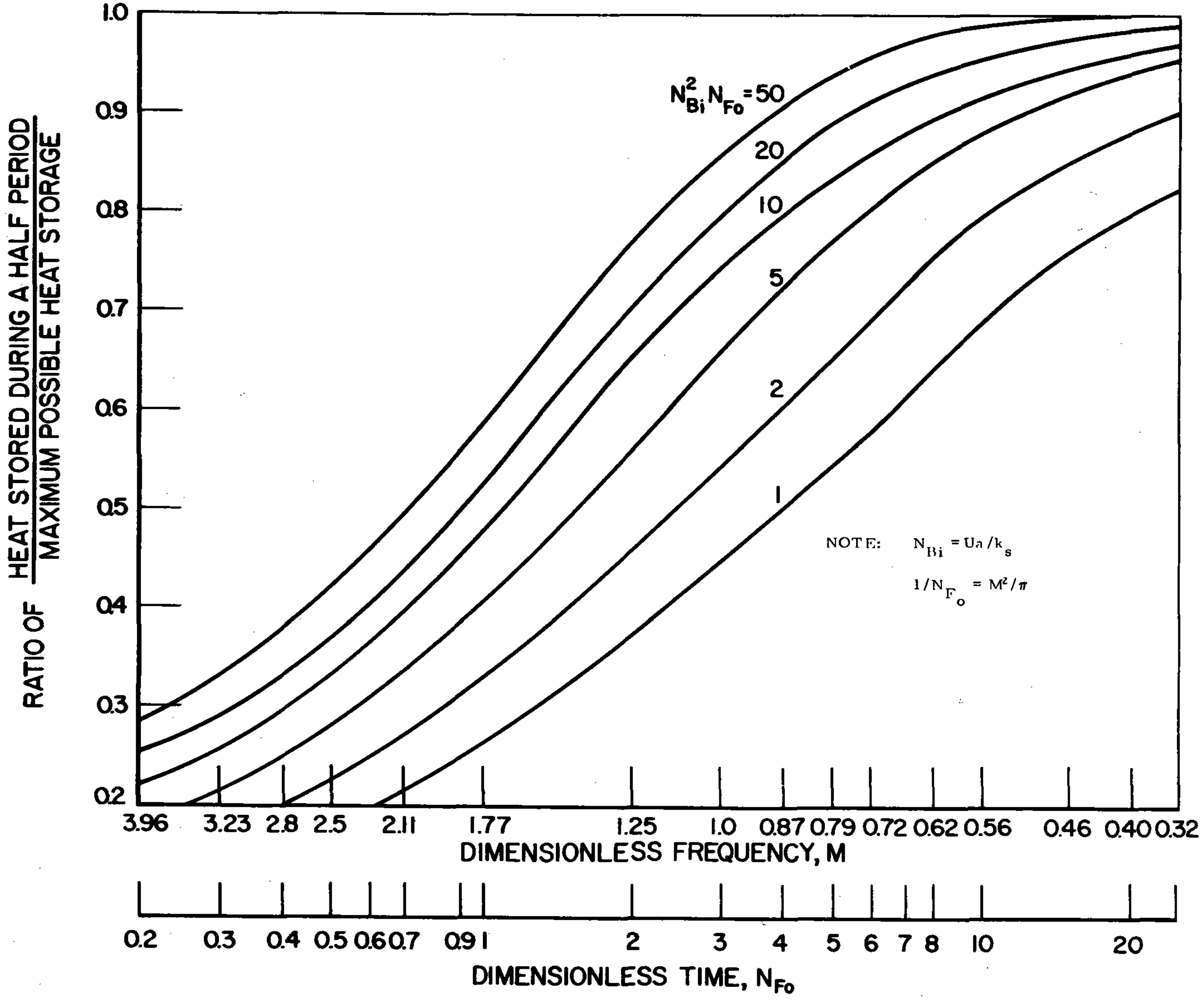

B77020499

Figure 2.2.9. ENERGY STORAGE IN A SLAB WITH PERIODICALLY VARYING AMBIENT TEMPERATURES

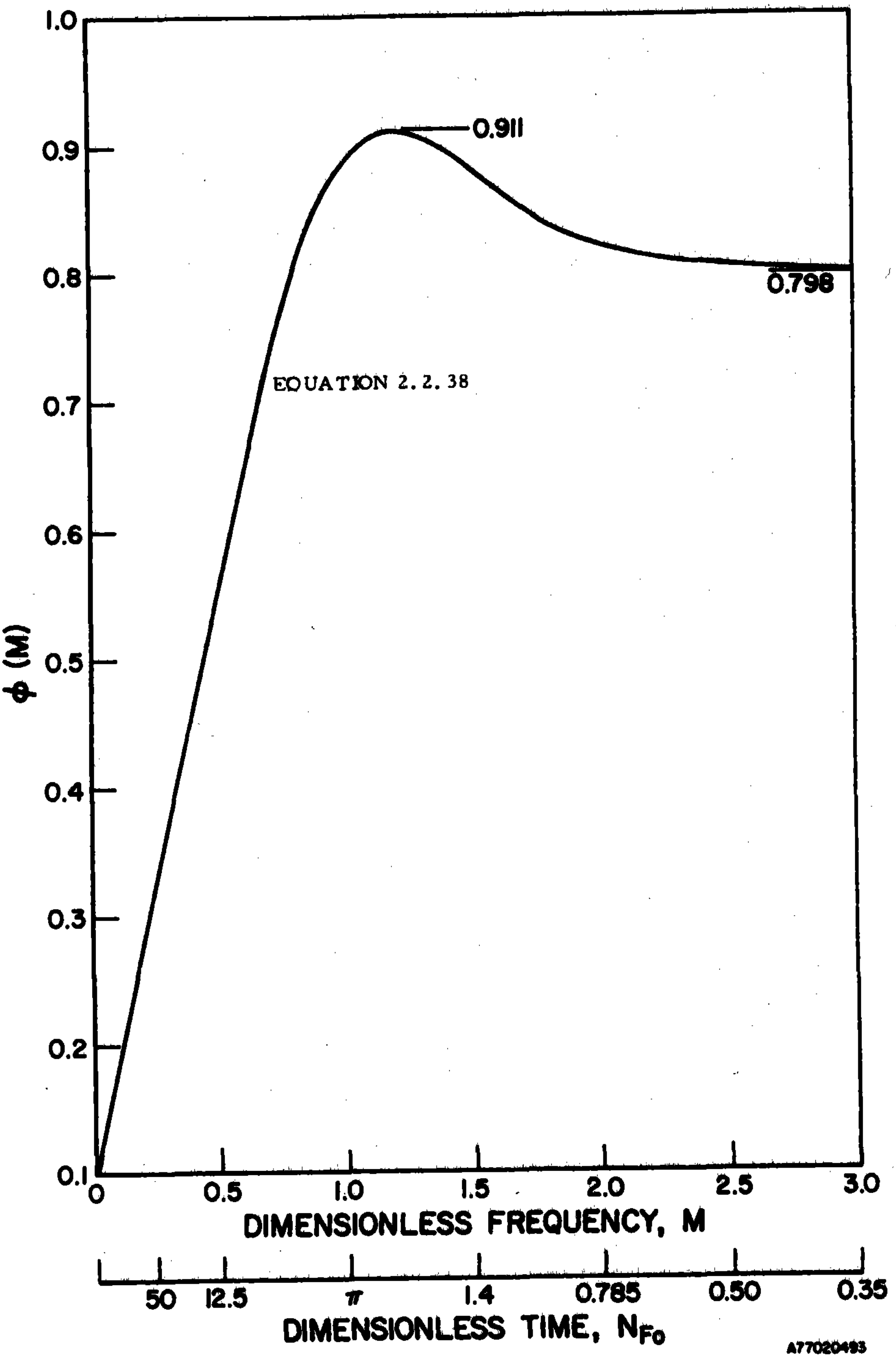

Figure 2.2.10. FUNCTION $\phi(M)$ DESCRIBING THE CAPABILITY OF A SLAB SUBJECTED TO HARMONIC SURFACE TEMPERATURE VARIATION TO STORE HEAT ENERGY DEPENDING ON ITS THICKNESS

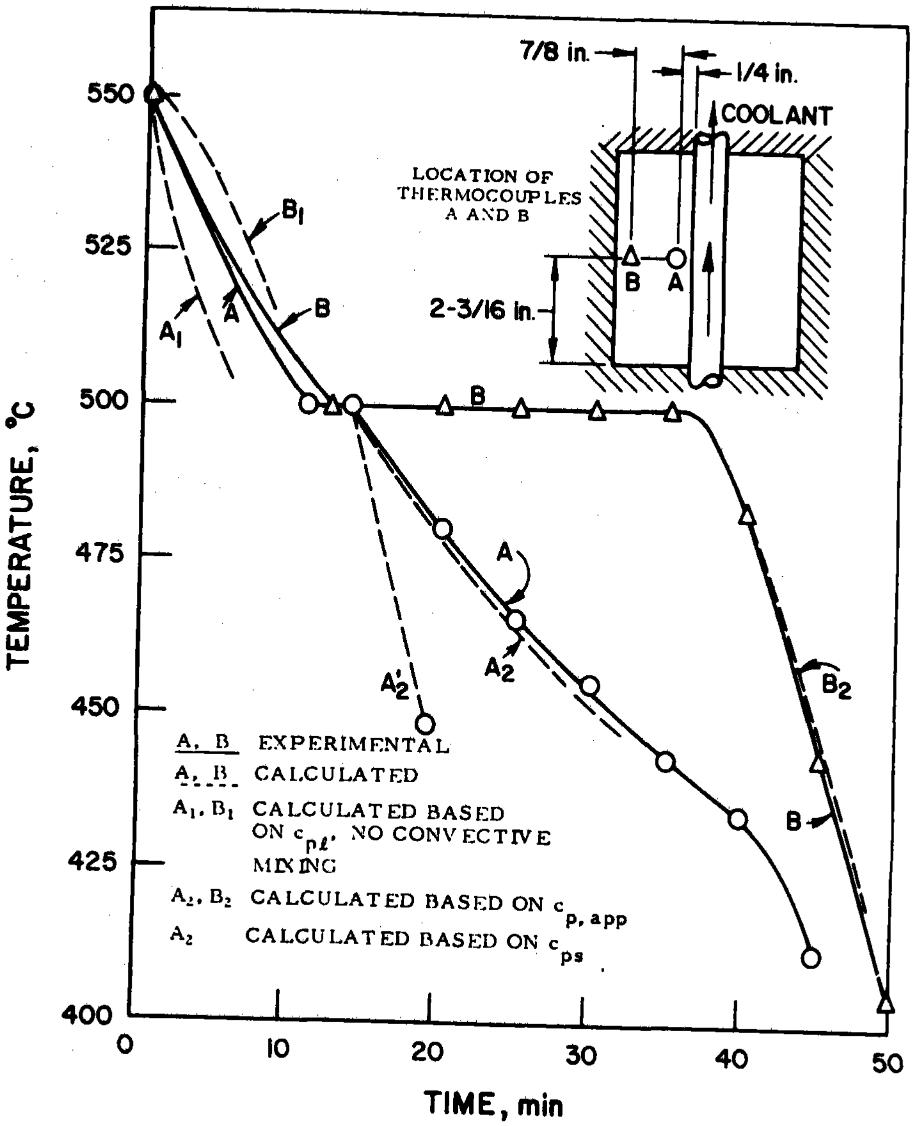

A77020502

Figure 2.2.11. COOLING RATES IN A PILOT TES UNIT (Run No. P7)

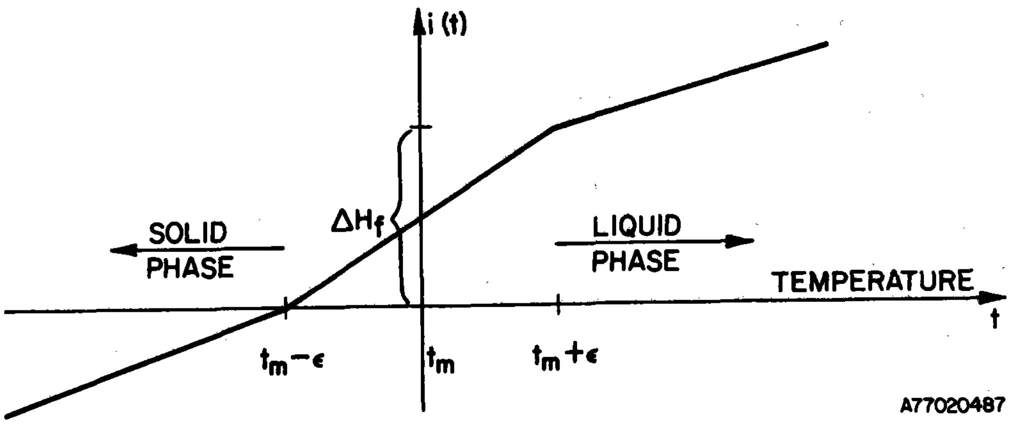

Figure 2.2.12. GRADUAL RELEASE OF THE LATENT HEAT (The "Slush" Condition)

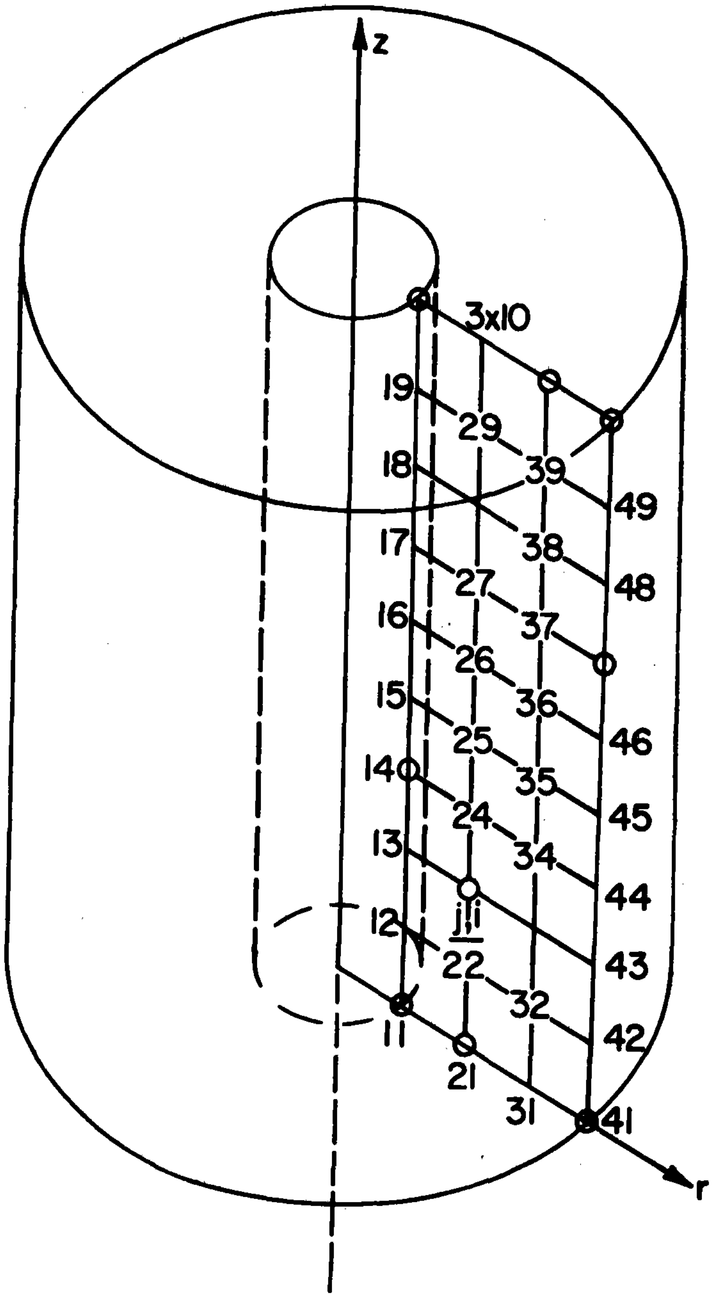

A77020488

Figure 2. 2. 13. FINITE DIFFERENCING GRID

2.3. VERIFICATION OF THERMOPHYSICAL PROPERTIES OF LiKCO$_3$ AND INVESTIGATION OF VOLUME CHANGE CONTROL ADDITIVE

The purpose of this task was to determine or verify certain thermophysical properties of LiKCO$_3$ critical to the performance of this salt as a heat of fusion-thermal energy storage material and to investigate the feasibility of using an inert support material, lithium aluminate (LiAlO$_2$), to minimize or eliminate on a macroscopic scale the volumetric expansion accompanying fusion of this salt. The salt properties selected for study were melting point, supercooling behavior, thermal expansion of the solid, and the volume change accompanying fusion. These studies also included the variation in melting point with thermal cycling, lithium aluminate additions, and contamination by corrosion products. The feasibility of using LiAlO$_2$ as a support material was assessed by examining the storage capacity sacrificed by the addition of LiAlO$_2$ and determining the rate at which the LiAlO$_2$ particles settle from the carbonate-aluminate paste. The results of these studies are discussed below.

2.3.1. Thermophysical Properties of LiKCO$_3$

The melting point of LiKCO$_3$ has been determined by Janz and Lorenz to be 504.5° ± 1° C.[12] However, Reshetnikov and Perfil'eva in Russia reported the melting point to be considerably lower, 474° C.[13] The source of this discrepancy has not been determined because of a lack of procedural details in the Russian work. A difference of this magnitude in the melting point of LiKCO$_3$ could have significant implications for the design and application of a thermal energy storage system using LiKCO$_3$ as the storage medium. Differential thermal analysis (DTA) and measurements of electrical conductivity as a function of temperature were made on mechanical and fused mixtures of Li$_2$CO$_3$ and K$_2$CO$_3$ corresponding in composition to LiKCO$_3$ to verify the melting points reported by these investigators. The DTA trace obtained from a mechanical mixture is shown in Figure 2.3.1A, and a trace from the same powder after fusion is shown in Figure 2.3.1B. Both of these traces show two endothermic ($\Delta T < 0$) peaks representing fusion. The first peak occurs at 480° C, representing the initial liquid formation at the solidus temperature (determined from several other runs as an average of 485° C, and reported by Janz and Lorenz[11] as 488° C). The second peak, occurring at

505^0 C in both traces, represents the fusion of $LiKCO_3$. The formation of a liquid phase (485^0 C) and the increase in the amount of liquid formed (505^0 C) were confirmed by electrical conductivity measurements, which showed a rapidly increasing electrical conductivity throughout this temperature range. We concluded from these results that the melting point of $504.5^0 \pm 1^0$C reported by Janz and Lorenz is the correct melting point.

Electrical conductivity measurements and DTA were also used to determine the influence of thermal cycling and the presence of lithium aluminate and corrosion products of 300 series stainless steel on the melting point of $LiKCO_3$. Figure 2.3.1C is a DTA trace obtained from $LiKCO_3$ with 17 weight percent $LiAlO_2$ added. Once again the trace shows two endothermic peaks at 487^0 and 505^0 C, indicating that the addition of lithium aluminate does not affect the melting point of $LiKCO_3$. DTA traces obtained from $LiKCO_3$ after it had been held molten in a Type 304 stainless steel container for periods of over 100 hours showed no deviation in the melting point even though the salt was discolored slightly by the corrosion products of the steel. However, a mixture of $LiKCO_3$ with 17 weight percent $LiAlO_2$ added showed a melting point between 496^0 and 500^0 C after containment in Type 304 stainless steel at 530^0 C for over 1200 hours. Whether this melting point depression is due to the presence of corrosion products, or the presence of both $LiAlO_2$ and the corrosion products together, has yet to be determined.

The effects of thermal cycling (repeated fusion and solidification) and cooling rate on the fusion-solidification characteristics of $LiKCO_3$ are shown in Figure 2.3.2. Figure 2.3.2. shows DTA traces obtained from the same salt as that in Figures 2.3.1A and 2.3.1B but after 12 fusion-solidification cycles. One distinct difference exists between the DTA traces in Figure 2.3.2 and those in Figure 2.3.1 – the absence of the solidus peak at 485^0C. The fact that this peak occurred in the traces in Figure 2.3.1 indicates that the initial composition was slightly richer in Li_2CO_3 than $LiKCO_3$. The absence of the solidus peak in Figures 2.3.2A and 2.3.2B indicates that the excess Li_2CO_3 has been lost by vaporization, corrosive reactions with the container, or some other mechanism. The single endothermic peak occurring at 505^0C indicates that the composition has corrected itself to that of $LiKCO_3$

with no variation in the melting point. It would, therefore, appear that thermal cycling has a stabilizing effect on $LiKCO_3$.

The effect of cooling rates on solidification is seen by examining the exothermic ($\Delta T > 0$) solidification peaks. Under a slow cooling rate (2^0 C/min) as shown in Figure 2.3.2B, solidification begins between 498^0 and 495^0 C, indicating a supercooling of the molten $LiKCO_3$ between 7^0 and 10^0 C. Under a faster cooling rate (7^0 C/min), solidification occurs at 507^0 to 505^0 C, as shown in Figure 2.3.2A. Since the cooling rates in a TES system are expected to be fast ($> 5^0$ C/min), supercooling of $LiKCO_3$ storage medium is not likely. When $LiAlO_2$ is added to $LiKCO_3$ to form a composite storage medium, supercooling is not observed at even slower cooling rates.

The thermal expansion and volume change occurring on fusion of a PCM are important because of the demands they place on containment materials and design. Containment vessels must be constructed to allow for the volume changes accompanying heat-up and fusion of the storage medium. The thermal expansion of solid $LiKCO_3$ was determined from hot-pressed samples having densities of 2.20 g/cu cm ($\approx 99\%$ theoretical density of $LiKCO_3$). The thermal expansion was found to be linear with temperature and showed a dependence on the pressing direction: the measured expansion coefficients are $3.4 \times 10^{-5}/^0$C parallel to the pressing direction and $2.8 \times 10^{-5}/^0$C perpendicular to the pressing direction. The density of solid $LiKCO_3$ at its melting point was calculated from these expansion coefficients to be 2.13 g/cu cm, representing a volumetric expansion of 4.4% from room temperature to 505^0 C. The density of liquid $LiKCO_3$ can be estimated from data of Spedding[14] as 2.01 g/cu cm at the melting point. The volume change on fusion of $LiKCO_3$ was calculated from these density differences to be 6%. Therefore, a total volumetric expansion of approximately 10.5% must be allowed for in containment design.

2.3.2. Volume Control Additives

The containment of a PCM used as a thermal energy storage medium is complicated by the differences in thermal expansion between the containment material and the PCM and the volume change accompanying fusion of the PCM. These differences in thermophysical behavior between storage and containment materials can lead to more complex containment design, increased containment cost, and lower volumetric storage capacity (based on container size). Each of these effects can decrease both the practicality and efficiency of thermal energy storage utilizing the heat of fusion of a PCM. The thermophysical properties of a PCM alone cannot be modified or controlled. However, they can be substantially reduced by creating a composite storage material containing both the PCM and an inert support material. The support material is characterized by its stability, thermal expansion, and particle size and morphology. The material is selected so that its thermal expansion is considerably lower than that of the PCM, thereby producing a composite thermal expansion lower than that of the PCM alone. Furthermore, the particle size distribution and morphology must be such that loosely packed particles form a tight, continuous capillary network. When the PCM is molten, all of the void space within the support matrix is filled with the liquid. As the PCM solidifies and undergoes the accompanying volumetric contraction, the capillary network serves to localize the resulting voids on a microscopic scale, within the capillaries. The net effect is to distribute the void space (resulting from the PCM volume change on solidification) throughout the composite storage medium. Therefore, on a macroscopic scale, the volume change accompanying a phase change and the void space required to accommodate it are barely detectable. As a result, any void formation or break-away from the heat transfer surfaces can be minimized. A closed containment vessel filled with a composite storage medium would not be subjected to the stresses induced by volumetric expansions and contractions accompanying fusion and solidification of the PCM. Therefore, associated complications in containment design and structure are eliminated. The incorporation of a support material into a storage medium is disadvantageous in that the storage capacity lost by the displacement of the PCM is only partially recovered as sensible heat storage in the support material.

We have selected $LiAlO_2$ as a support material because:

- The PCM being studied ($LiKCO_3$) is in the lithium carbonate-potassium carbonate system; the chemical inertness of $LiAlO_2$ to components in this system has already been proven;[15,16]

- The coefficient of thermal expansion of $LiAlO_2$ is approximately one-third that of $LiKCO_3$; and
- The ability of this material to develop the required capillary network has been displayed in past work at IGT.[17]

The effects on storage capacity (Btu/lb) and specific capacity (Btu/cu ft) of lithium aluminate additions to $LiKCO_3$ are shown in Figure 2.3.3. Capacity values for the composite storage medium were calculated for a 100^0 C cycling ($505^0 \pm 50^0$ C). Under these conditions, the storage capacity of pure $LiKCO_3$ is 224 Btu/lb (148 Btu/lb as the heat of fusion and 76 Btu/lb as sensible heat). It is estimated that $LiAlO_2$ must be added in excess of 30% by weight to effectively control the volume change on fusion of $LiKCO_3$. The storage capacity of the composite is reduced to 170 Btu/lb with $LiAlO_2$ added in this amount. This composite represents a 24% decrease in storage capacity and a 17.5% decrease in specific capacity from that of $LiKCO_3$ alone. More important is the effect of $LiAlO_2$ additions on capacity cost. The capacity cost of $LiKCO_3$ operating under a 100^0 C cycling is $\$1,790/10^6$ Btu.* A composite storage medium containing 30 weight percent $LiAlO_2$ and 70 weight percent $LiKCO_3$ operating under the same 100^0 C cycling would have a capacity cost of $\$6,150/10^6$ Btu, a 244% increase.†

Another difficulty anticipated is maintaining a uniform distribution of the support material throughout the composite. If the support material settles out of the composite, the capillary network needed to control the volume change accompanying fusion of the PCM is destroyed. As the support material settles, the volumetric changes of the composite with cycling increase. This may cause undesirable voids and a safety hazard if the storage container design is based on the expansion of the composite containing an even distribution of the support material. The particle size and density of the support material and the viscosity and density of the liquid in which the particles are suspended determine the rate at which the particles will settle through the liquid. $LiAlO_2$ has a density of 2.6 g/cu cm (primarily β and γ crystalline phases); molten $LiKCO_3$ has a density of 2.0 g/cu cm and a viscosity of 10 to 15 cP near the melting point.

---

* Salt prices taken from <u>Chemical Marketing Reporter,</u> (1976) Nov. 29.

† $LiAlO_2$ price obtained from Lithium Corporation of America, 1976 listing; \$2.55/lb.

Stoke's law was used to estimate the settling rate of $LiAlO_2$ through molten $LiKCO_3$ as a function of $LiAlO_2$ particle size and is shown in Figure 2.3.4. Sedimentation tests were conducted on a composite mixture containing 83 weight percent $LiKCO_3$ and 17 weight percent $LiAlO_2$ having a particle size distribution between 0.01 and 0.2μ diameter. The powder was packed into Type 304 stainless steel columns 1-1/4 inches in diameter and 12 inches deep. The columns were then heated to 530^0 C and air quenched after 300, 700, and 1250 hours, respectively, at these temperatures. Samples were then taken from the uppermost and lowest centimeter depth, and the $LiAlO_2$ concentration was determined. The results of this test are shown in Figure 2.3.5. The settling rate calculated from Stoke's law for the average particle size of the $LiAlO_2$ used in this test was 3 mm/1000hr. The settling rate determined from this test was 8 mm/1000 hr. Stoke's law, however, assumes that no interaction between particles occurs during settling. The effect of particle flocculation is to increase the settling rate, because the apparent particle size is increased. It may, therefore, be concluded that flocculation is occurring at the initial $LiAlO_2$ concentration. After 1250 hours, the $LiAlO_2$ concentration in the top of the column has been reduced by nearly 100% although the $LiAlO_2$ concentration in the bottom of the column has only increased by 50%. It appears that, as the $LiAlO_2$ concentration increases from 17 weight percent, hindered or compression settling is occurring. This indicates that the calculated settling rate of 8 mm/1000 hr represents a maximum settling rate, which would decrease significantly as the initial concentration of $LiAlO_2$ is increased from 17 weight percent.

In addition to the problems of reducing the storage capacity and high cost, adding $LiAlO_2$ to $LiKCO_3$ can also hinder the heat transfer characteristics. A composite storage medium containing 3 percent by volume $LiAlO_2$ in $LiKCO_3$ was tested in the pilot TES system* to study this effect. The results are included in Table 2.4.1 for comparison with pure $LiKCO_3$ and $LiKCO_3$ with conductivity promoters added. Taking pure $LiKCO_3$ as a standard for comparison shows the heat recovery (Q_t/Q_s) reduced from 68% to 66% by the addition of $LiAlO_2$ at this level, and the heat flux reduced from

---

* Details of the pilot TES system are presented in Sections 2.2 and 2.4.

9,280 to 9,215 Btu/hr-sq ft. Although these changes are small, they indicate the decrease in overall system efficiency resulting from the addition of $LiAlO_2$ to the $LiKCO_3$.

The decrease in storage capacity and system efficiency and the increase in capacity cost resulting from $LiAlO_2$ additions represent disadvantages of the use of $LiAlO_2$ as a volume control additive. Because the volume change of $LiKCO_3$ in our system is $< 10\%$, the benefits to be derived from volume change control additive may be less important compared with the accompanying disadvantages. However, if a high volume-change system (such as chlorides) is used, the volume control additive may become important. Our studies of volume control additives will therefore be restricted to study of the concept, rather than its application to our specific system.

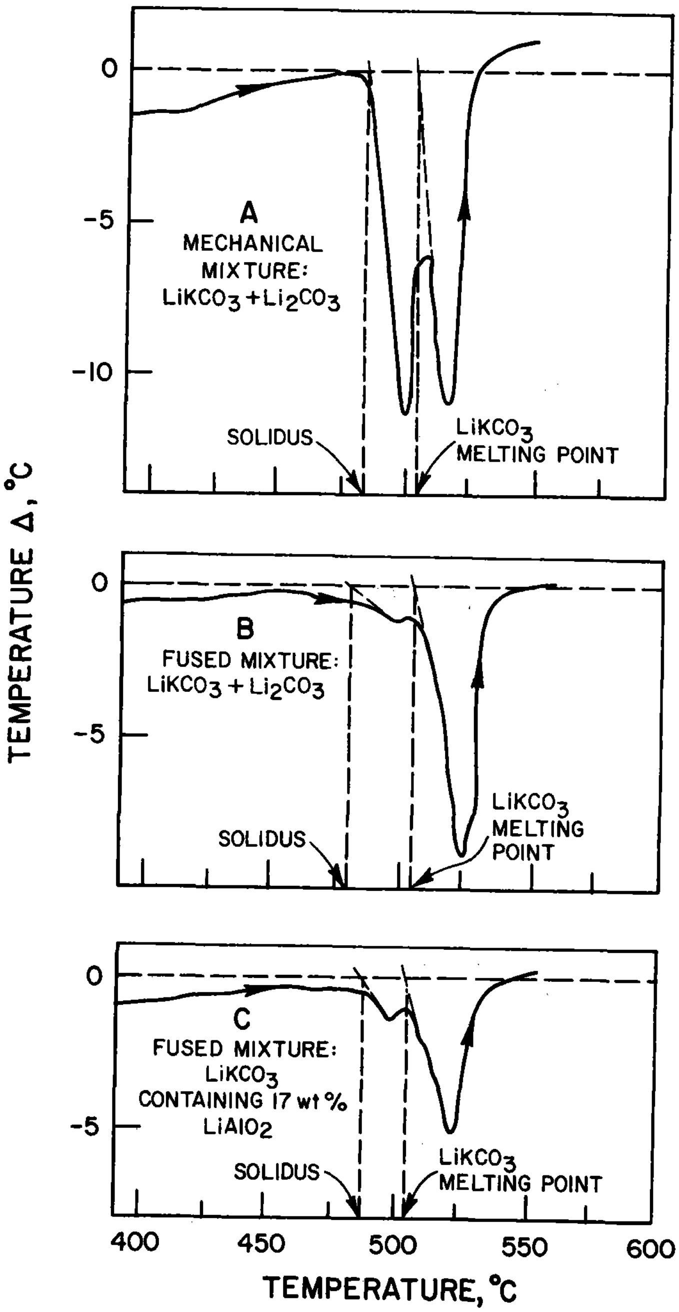

A77020501

Figure 2.3.1. DTA TRACES OF MECHANICAL AND FUSED MIXTURES OF $LiKCO_3$

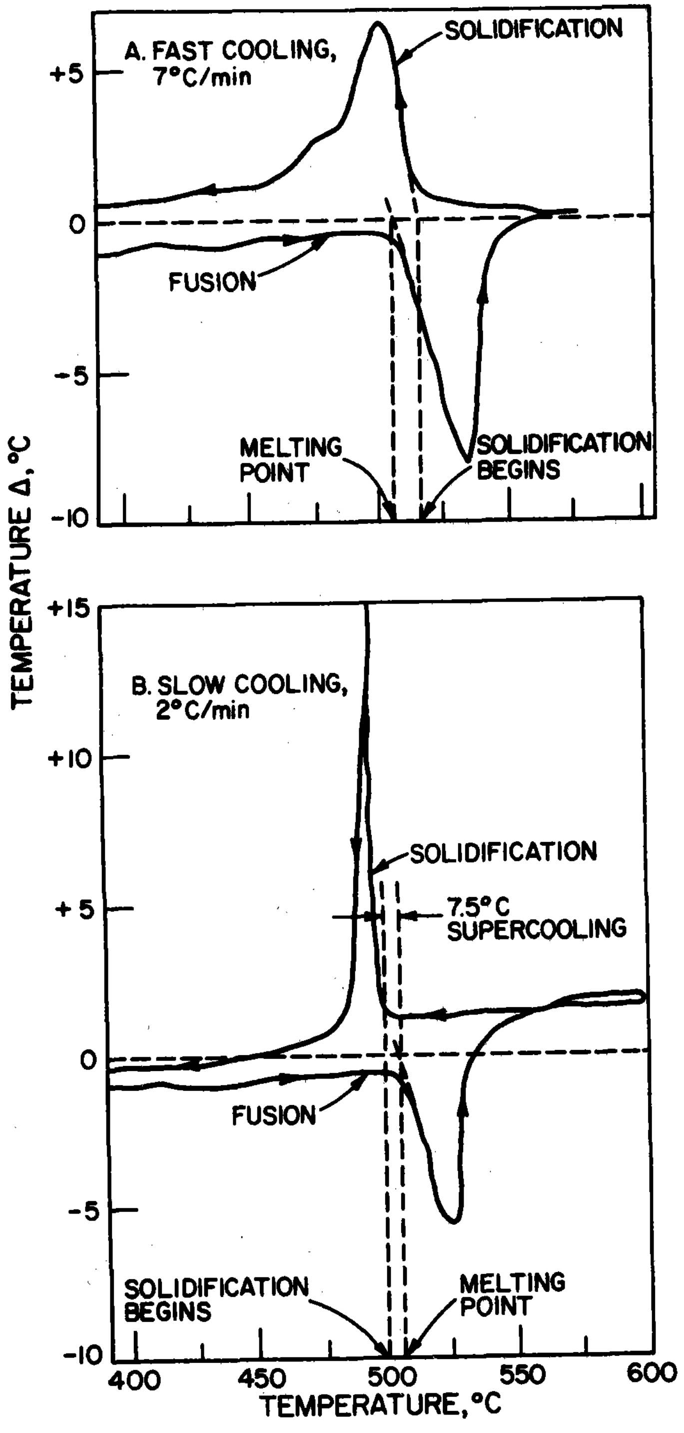

A77020500

Figure 2.3.2. DTA TRACES OF THERMALLY CYCLED $LiKCO_3$

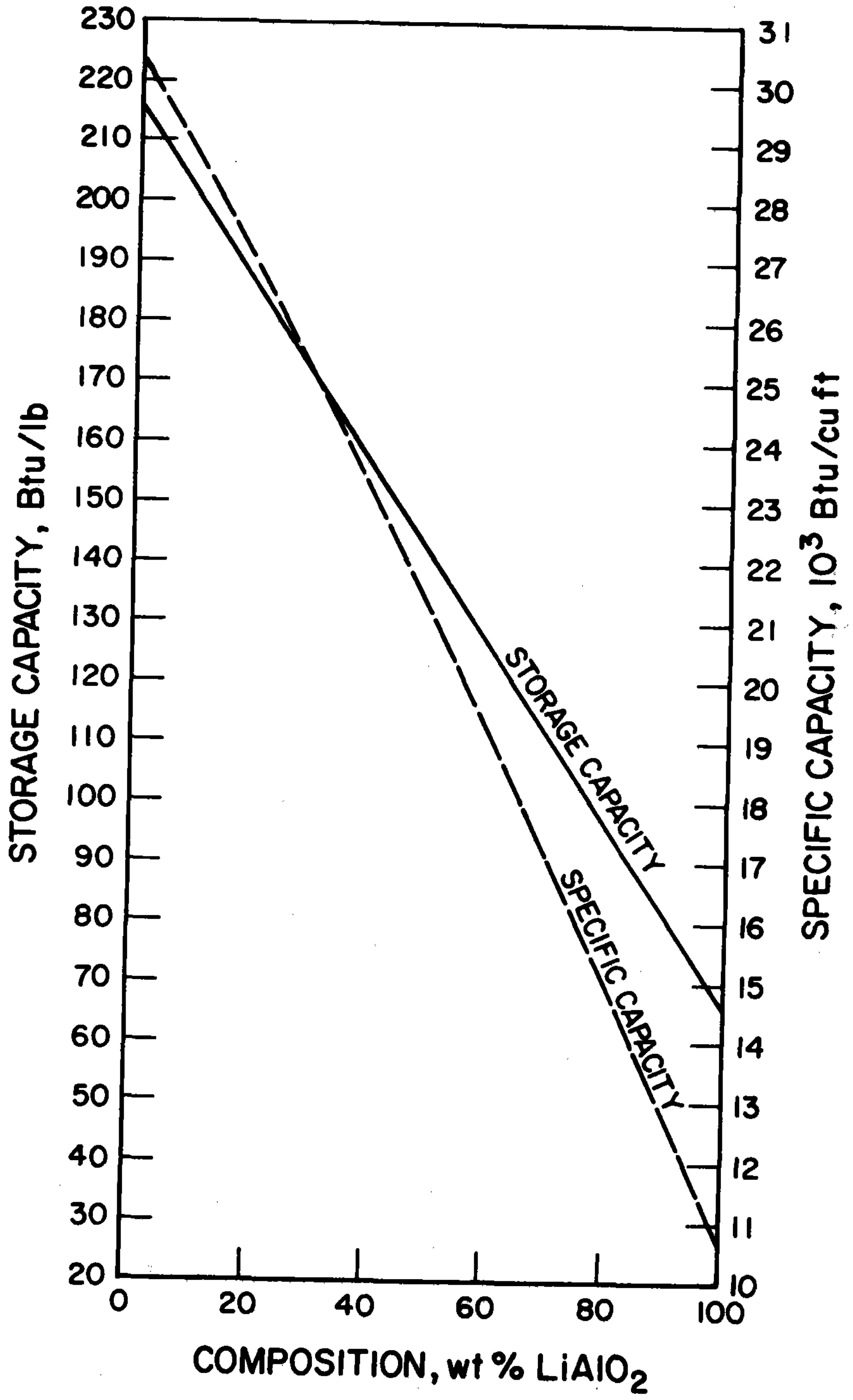

Figure 2.3.3. CAPACITY VARIATION WITH COMPOSITION OF $LiKCO_3$-$LiAlO_2$ COMPOSITE STORAGE MEDIUM

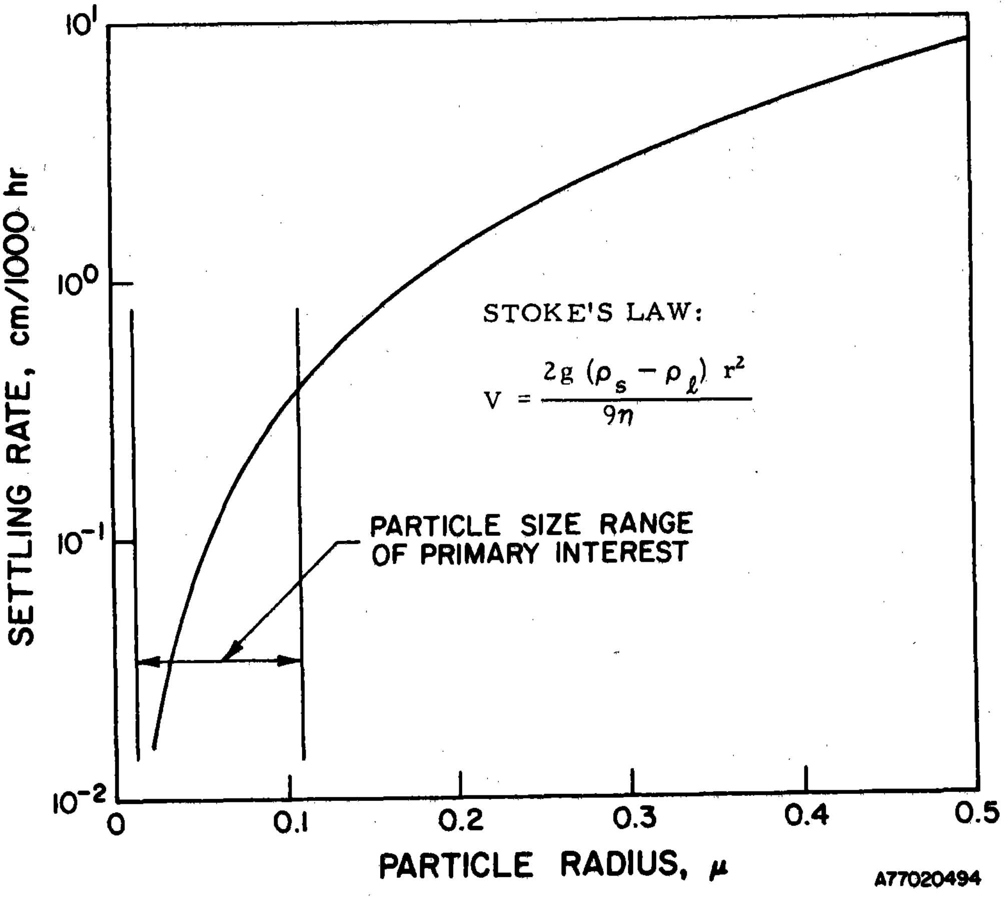

Figure 2.3.4. CALCULATED SETTLING RATE OF $LiAlO_2$ IN MOLTEN $LiKCO_3$ AT 525°C

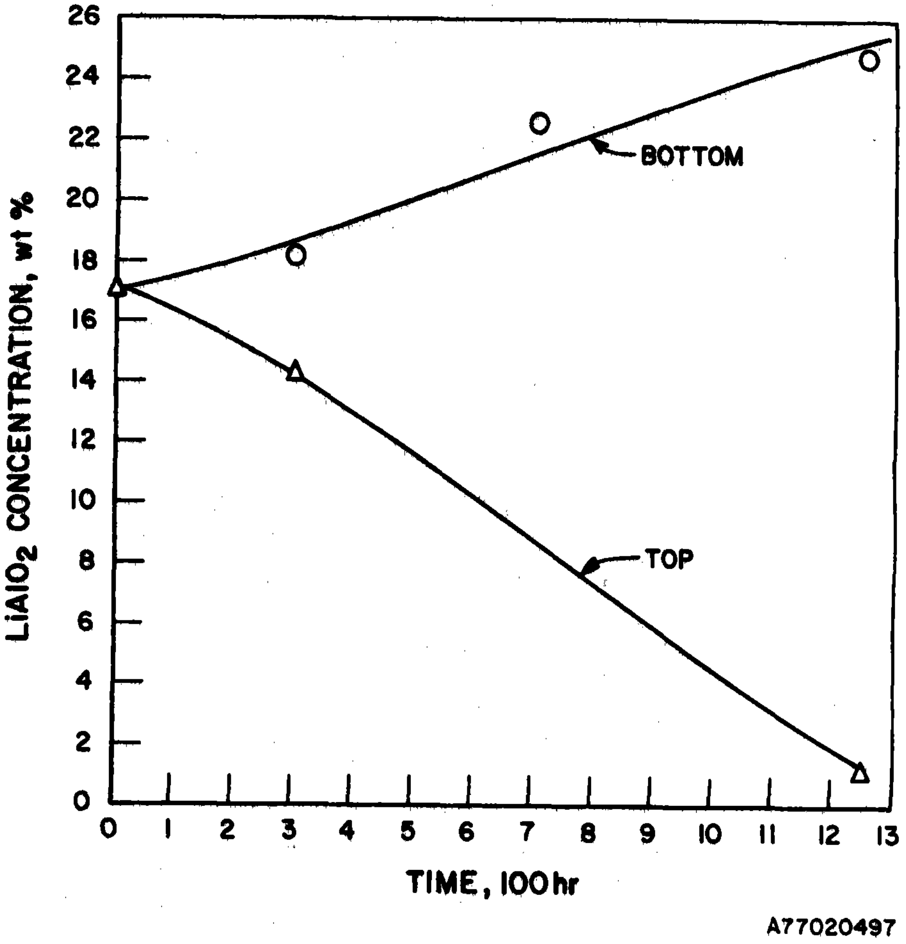

Figure 2.3.5. OBSERVED SEDIMENTATION OF $LiAlO_2$ IN MOLTEN $LiKCO_3$ AT 530° C

2.4. INVESTIGATION OF CONDUCTIVITY PROMOTERS

As we reported in Task 1 Report[3] alkali metal carbonates have relatively high thermal conductivities (~1 Btu/hr-ft-°F), compared with various inorganic salts considered. However, noting that heat transfer area required for a given quantity of heat depends strongly on thermal conductivity (particularly in the solid region of the salt), the heat transfer area and the resulting cost of the storage system can be minimized if the conductivity of the salt medium can be improved. We therefore investigated the use of high-conductivity materials as conductivity promoters. Considerations for the selection of suitable conductivity promoters include—

1. Thermal conductivity and heat capacity
2. Compatibility with carbonates
3. Availability
4. Suitability of fabrication in desirable forms
5. Cost.

After the initial considerations, different materials in various shapes were experimentally tested in our pilot TES (3-inch diameter container) unit. Their results will be discussed here.

2.4.1. Materials and Configurations for Conductivity Promoters

Several materials suitable for the conductivity promoter are shown in Table 2.4.1, along with their thermal conductivities, heat capacities, and approximate costs.

Aluminum is the most attractive material for a conductivity promoter because of its high thermal conductivity and low cost. It can be fabricated in various configurations including honeycomb matrix, wool, and screens. Its corrosion resistance is reasonable because it forms a protective alumina layer (Section 2.5). The thermal conductivity of Al_2O_3 is 2 orders of magnitude smaller than that of aluminum, but because only a thin film of Al_2O_3 is formed, the overall decrease in conductivity may not be significant. This factor, however, should be considered in the design of a conductivity promoter. Another important point is that the melting point of aluminum is 660° C, approximately 100° C above the maximum temperature anticipated in the $LiKCO_3$ TES system. Thus aluminum may be structurally weak.

Table 2.4.1. PROPERTIES OF MATERIALS CONSIDERED AS CONDUCTIVITY PROMOTERS

Material	Thermal Conductivity, Btu/hr-°F-ft		Heat Capacity Btu/lb-°F		Material Cost,		Remarks
	at 100°C	at 500°C	Room Temp	at 500°C	$/lb	$/cu ft	
Type 304 L SS	9.4	12.5	0.12	--	0.948	475	
Type 316 SS	9.4	12.5	0.12	--	1.273	638	
Type 347 SS	9.3	12.9	0.12	--	2.510	1258	Best corrosion resistance of 300 series SS
Type 430 SS	15.1	15.2	0.11	--	0.841	421	
Type 446 SS	12.1	14.2	0.12	--	2.555	1192	
Aluminum	136	127	0.22	0.27	0.792	134	660°C mp; may become soft if temp of system increases accidentally.
Pyrolytic Graphite	300	120	~ 0.2	--	924.00	130,000	As deposit; thermal conductivity was measured parallel to basal plane
Graphite ATJ	65	43	0.2	0.38	4.47	626	Thermal conductivity was measured parallel to grain
Graphite CS	70	44	0.2	0.38	0.50	68	0% porosity

Additionally, if system upsets occur that increase the system temperature to close to the melting point of aluminum, a complete collapse of aluminum is possible. Therefore, if aluminum is selected as a construction material, precautions to guard against accidental temperature increases are essential.

Stainless steels have lower thermal conductivities than aluminum (12 to 15 Btu/hr-ft-°F), but they have some advantages. Stainless steel is reasonably stable in the carbonate environment (Section 2.5), and stainless steel in the shape of wool, foam, honeycomb matrix or expanded metal can be easily attached to the heat transfer surface (heating or cooling tube), which may result in a higher heat transfer rate. Use of foam or wool can also localize the void formation, thereby minimizing the heat transfer problem. Screen is another configuration of interest, but welding is required to attach it to the heat transfer surface, which leads to a higher labor cost.

Graphite seems to be an attractive material because of its high conductivity, although the conductivity varies for different grades of graphite. Because the density of graphite ($\sim$2.25 g/cu cm) is very similar to that of carbonates ($\sim$2 g/cu cm), graphite can also be used in particulate form, so that it can act as volume-change control additive as well. Only a small amount of settling (compared with $LiAlO_2$, discussed in Section 2.3) would be expected in this case. The stability of graphite, however, needs to be investigated.

2.4.2. Testing of Conductivity Promoter Materials

To obtain relative improvements in heat-transfer rates with the addition of conductivity promoter, we tested some available materials in our pilot TES system. Figures 2.4.1 and 2.4.2 show the constructional details and location of thermocouples in the system. A 3-inch-diameter, 5-inch-long stainless steel tube, with the bottom end sealed, containing 800 grams of 35 weight percent Li_2CO_3 -65 weight percent K_2CO_3 ($LiKCO_3$) was heated in an electrical furnace with a heat input of 9A at 115V (heating rate of approximately 5^0 C/min). After the carbonate reached the equilibrium temperature, the cooling air (50 ft/s) was fed from the bottom of the 1/2-inch OD center tube. Baseline salt cooling characteristics have been established and analyzed in Section 2.2. Heat-up and cooldown cycles have also been conducted for $LiKCO_3$ with: a) 3% by volume stainless steel screen attached to the center cooling tube, b) 3% by volume aluminum honeycomb matrix immersed in the salt, and c) 3% by volume stainless steel wool immersed in the salt. Temperature responses versus cooling time of the pilot TES unit without any conductivity promoters and with the screen, honeycomb, and wool are plotted in Figures 2.4.3 through 2.4.5.

The following observations can be made from comparing these responses:

- Behavior in the Liquid $LiKCO_3$ Region. For the convenience of discussion, this region may be defined in the time period between 0 minutes, when cooling air is introduced, and 10 minutes, when most of the thermocouples show salt temperatures slightly above 500° C, although some of the salt near the center cooling tube has solidified.

  In this region, near the vicinity of the central wall (~1/4 inch), the liquids with the conductivity promoters cooled down faster than the liquid without the conductivity promoter. Among the liquids with three different conductivity promoters in this region, the one with stainless steel wool shows the fastest cooling rate, and the liquid with aluminum honeycomb has a faster cooling rate than the one with the stainless steel screen. Further away from the central wall (~1/2 inch), the cooling rate for the salt with conductivity promoters is somewhat slower than that for the salt with no conductivity promoter; also the salt with stainless steel screen has a somewhat faster cooling rate than the one with an aluminum honeycomb. The liquid with stainless steel wool in this area has the slowest cooling rate.

  The faster cooling rates near the inner wall may be caused by the improvements due to the conductivity promoters. The slower cooling rates near the outer wall may be explained by the inhibition of convective currents due to the presence of conductivity promoters.

- Behavior in the Partially Solidified $LiKCO_3$ Region. This region can be defined approximately as the time period between 10 and 35 minutes. Before about 10 minutes, most of the salt in the container is in the liquid phase. After about 35 minutes, the salt is considered completely solidified.

  In this region, the salt with an aluminum honeycomb matrix has a slower cooling rate than the salt with no conductivity promoter except in the near vicinity of the central cooling tube (~1/4 inch). Salt with stainless steel wool, at about 1/4 inch radial distance from the central cooling tube, has the fastest cooling rate. In this same area, the heat transfer rate for the salt with stainless steel screen is between that of the salt with no conductivity promoter and that of the salt with stainless steel wool. Further away from the central cooling wall (about 1/2 inch), the salt with no conductivity promoter shows the fastest cooling rate.

  The behavior again, can be explained by the inhibition of convective currents, especially in the case of the honeycomb matrix.

- Behavior in the Solid $LiKCO_3$ Region. Before 35 minutes, the thermocouples indicate a high temperature for the salt with the aluminum honeycomb. However, when (after 35 minutes) the salt is completely solidified, the cooling rate increases and surpasses that of the salt with the stainless steel screen and that of the salt with no conductivity promoter. This can be explained by the much higher thermal conductivity of aluminum relative to stainless steel and salt. Hence, after the salt solidifies, conduction becomes the primary mode of heat transfer. The high thermal conductivity of the aluminum results in a faster cooling rate. The same reasoning can also be used to explain the effect of the stainless steel screen. However, the salt with stainless steel wool still shows the best heat transfer rate. A possible explanation is the high surface to volume ratio of this particular configuration, which results in more heat transfer surface per unit volume for the stainless steel wool.

2.4.3. Improvement of Heat Flux and Trade-offs with Storage Capacity

The improvement of the heat transfer rate obtained by adding conductivity promoters to the $LiKCO_3$ can be observed quantitatively by studying the registered exit air temperatures, as shown in Figure 2.4.6.

The actual heat extracted by cooling air, and the theoretical maximum heat that can be extracted from $LiKCO_3$ with or without conductivity promoters, in the operating range of 550^0 to 450^0 C, were calculated (Table 2.4.2). Forty minutes after the cooling started, 68% of the available heat from $LiKCO_3$ with no conductivity promoter was transferred to the cooling air. By comparison, 75% of the available heat was transferred to the cooling air with stainless steel screen immersed in the salt, 81% was transferred to the air from the salt with aluminum honeycomb matrix, and 87% was transferred to the air from the salt with stainless-steel wool.

These improvements appear encouraging, but cannot be easily extrapolated because theoretical analysis of the complicated geometries is very difficult. One can resort to idealized geometries or calculate an effective overall conductivity from mixture rules,[18,19] but we have assumed that benefits derived from 3 volume percent conductivity promoters may be extrapolated linearly. Note that the results presented here are strictly applicable to the pilot TES system only, and a scale-up of these results to larger units needs verification.

Figure 2.4.7 shows the heat flux (Btu/hr-sq ft) and specific storage capacity (Btu/cu ft) versus the volume percentage of conductivity promoter present in $LiKCO_3$. Adding 23% by volume of stainless steel wool in the salt, for instance, reduces the storage capacity about 15% and increases

Table 2.4.2. COMPARISON OF HEAT-TRANSFER RATES TO COOLING AIR FROM LiKCO$_3$ WITH OR WITHOUT ADDITIVES (Conductivity Promoters and Volume Control Additives)

Description	Air Temp, °C		Air Mass Flow Rate, lb/min	Operating Temp Range, °C	Q_s,[b] Btu	Q_t,[c] Btu	q.[d] Btu/hr-sq ft	Q_t/Q_s, %
	T_{in}	T_{out}[a]						
LiKCO$_3$	24	97	0.224	545-450	413	281	9281	68
LiKCO$_3$ with 3 vol % of SS Screen	26	106	0.222	547-450	420	313	10,340	75
LiKCO$_3$ with 3 vol % of Aluminum Honeycomb	27	116	0.222	542-450	412	335	11,060	81
LiKCO$_3$ with 3 vol % of SS Wool	25	119	0.224	548-450	420	365	12,055	87
LiKCO$_3$ with 3 vol % LiAlO$_2$	24	97	0.224	550-450	424	279	--	66

[a] $T_{out} = \frac{1}{\Delta t}\int_{t=0}^{t=40} T(t)\,dt$, where

T_{out} = integrated temperature of exit air (See Figure 2.4.6.)

t = time

Δt = period of time.

[b] $Q_s = m_s c_p(s)\,\Delta T + \Delta H \cdot m_s + m_m c_p(m)\,\Delta t$, where

Q_s = theoretical heat that can be extracted from pilot TES unit in the operating temperature range, 450° to 550°C.

m_s = mass of salt, 1.76 lb of LiKCO$_3$

$c_p(s)$ = specific heat of salt (solid or liquid)

ΔT = operating temperature range, °C

ΔT = heat of fusion, 148 Btu/lb for LiKCO$_3$

m_m = mass of conductivity promoter

$c_p(m)$ = specific heat of conductivity promoter.

[c] Q_t = actual heat transferred to cooling air from pilot TES unit in 40 minutes after cooling started.

[d] q = heat flux, Btu/hr-sq ft (cooling tube surface area = 6.54 sq in.)

B77020135

the heat flux three-fold. Comparing the improvement in the heat flux and the trade-off in the heat capacity, the advantage of adding a certain amount of conductivity promoter in the salt seems to be well justified. At this point, we understand that the values of heat flux presented in Table 2.4.2 and Figure 2.4.7 were based on air with the velocity of 50 ft/s at room temperature as a cooling medium. If we use oil or water as a cooling medium, or increase the cooling air velocity above 50 ft/s, or increase the surface to volume ratios of the cooling tube, the heat flux will be somewhat increased. Also note that the presence of conductivity promoters may inhibit convective currents in the liquid region, thereby slowing down the heat transfer rates in that region, although the average heat transfer rates are faster. System interface considerations are necessary for a detailed study of such trade-offs, but it may be stated that a properly designed conductivity promoter may allow us to minimize the inhibition of convective currents. Screens, compared to the honeycomb matrix, will be more desirable from this point of view. From the standpoint of the surface to volume ratio, the configuration of wool or foam would be more desirable. Aluminum possesses much higher thermal conductivity than stainless steel; thus aluminum wool or foam metal would be considered the best choice for a conductivity promoter. Further testing of these configurations in the pilot TES system and in our engineering-scale system will continue to determine the increase in heat transfer rates as a function of the volume percentage of conductivity promoters added.

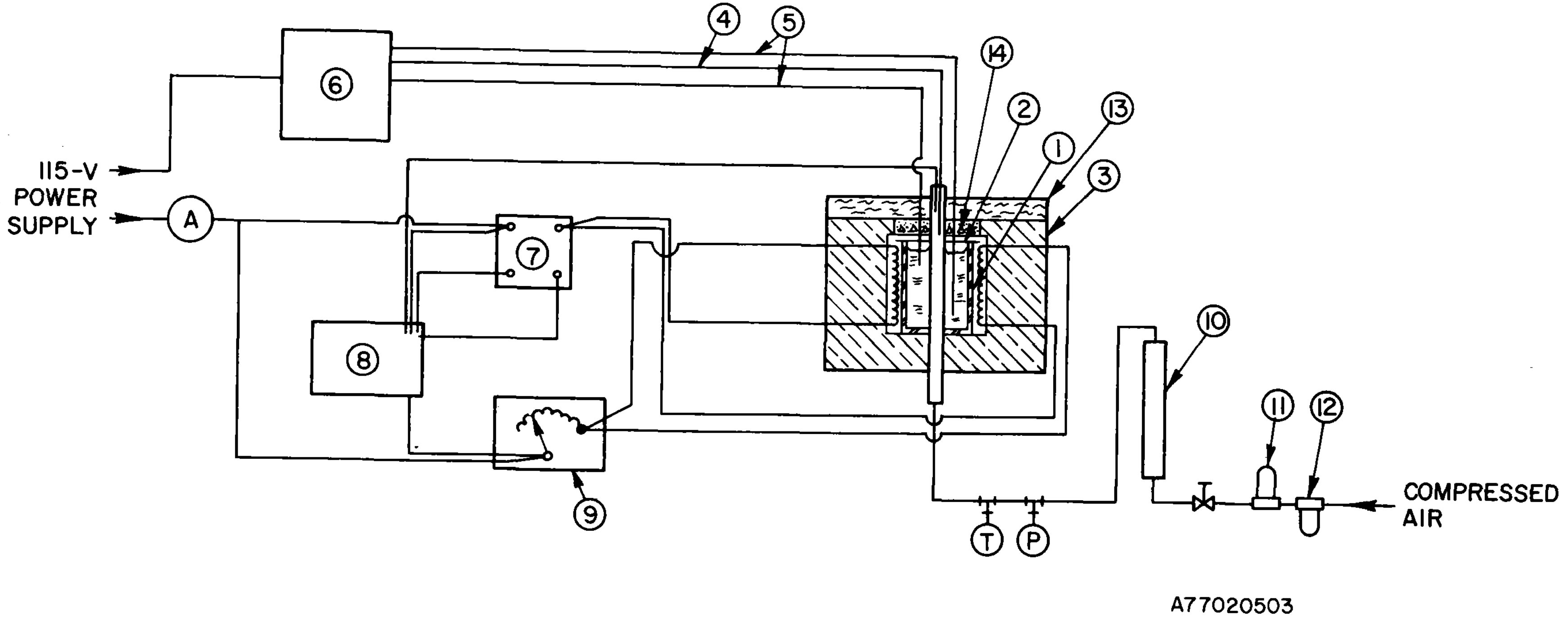

LEGEND

Item No.	Description	Item No.	Description
1	Pilot TES Container	9	Variable Transformer
2	Aluminum Sheet	10	Flowmeter
3	Electrical Furnace	11	Air Pressure Regulator
4	Thermocouple (Exit Aip Temp)	12	Air Filter
5	Thermocouples (Salt Temp)	13	Insulation Wool
6	Temperature Recorder	14	Brick Cap
7	Switch Relay		
8	Temperature Controller		

Figure 2.4.1. SCHEMATIC OF PILOT-TES SETUP

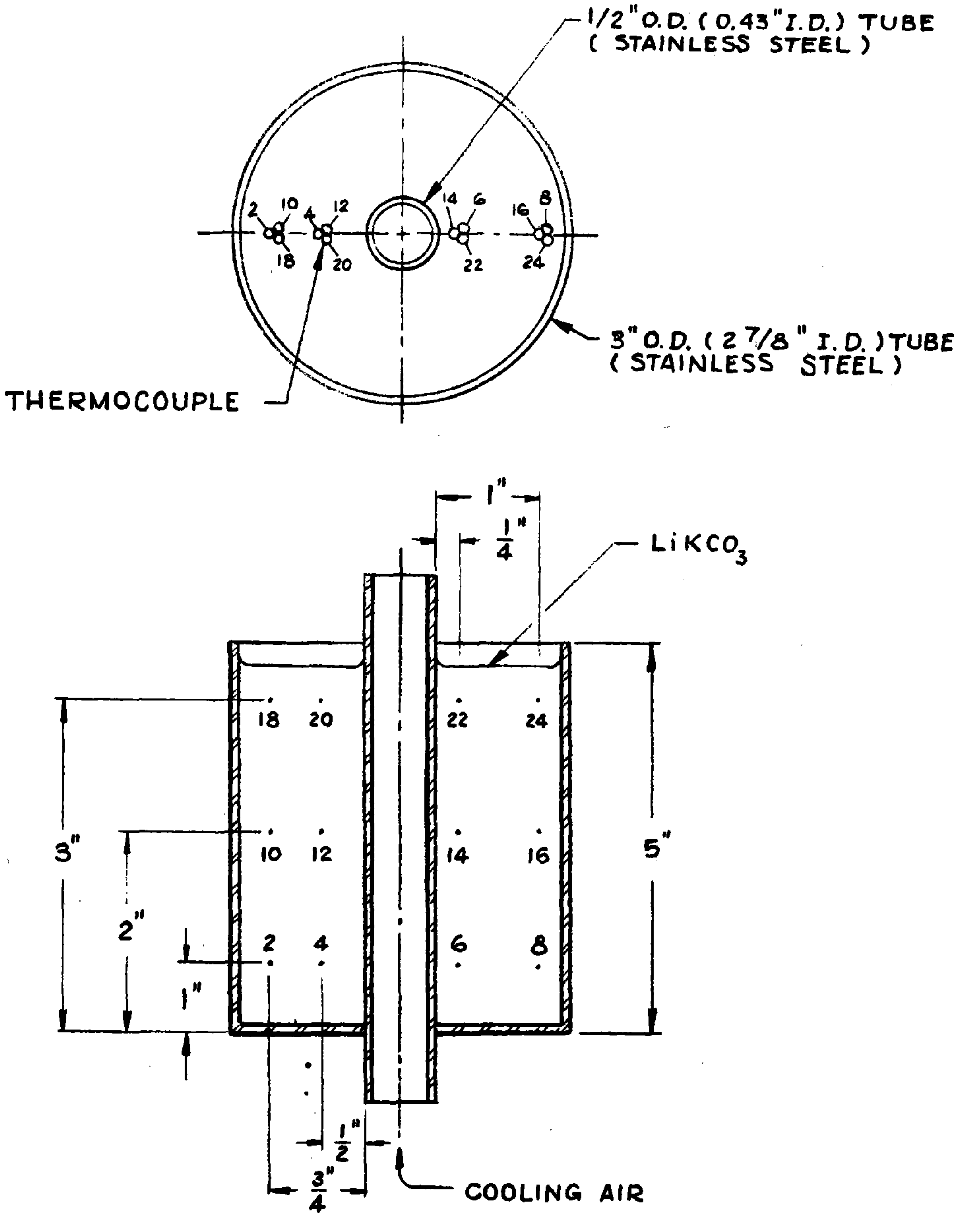

Figure 2.4.2 DIMENSIONS AND THERMOCOUPLE LOCATIONS IN PILOT-TES UNIT

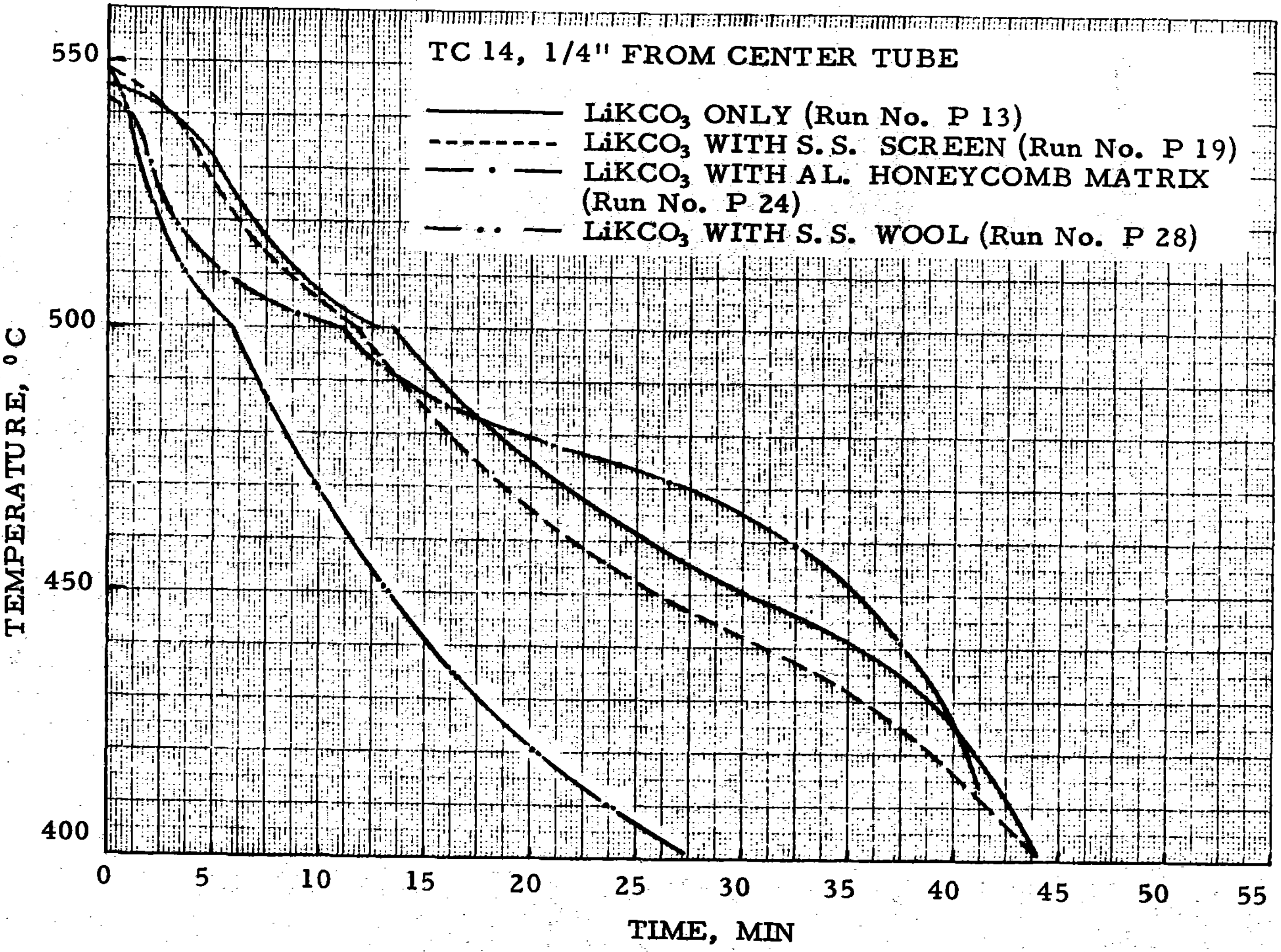

Figure 2.4.3 TEMPERATURE RESPONSES VERSUS TIME AT 1/4-INCH FROM CENTER COOLING TUBE

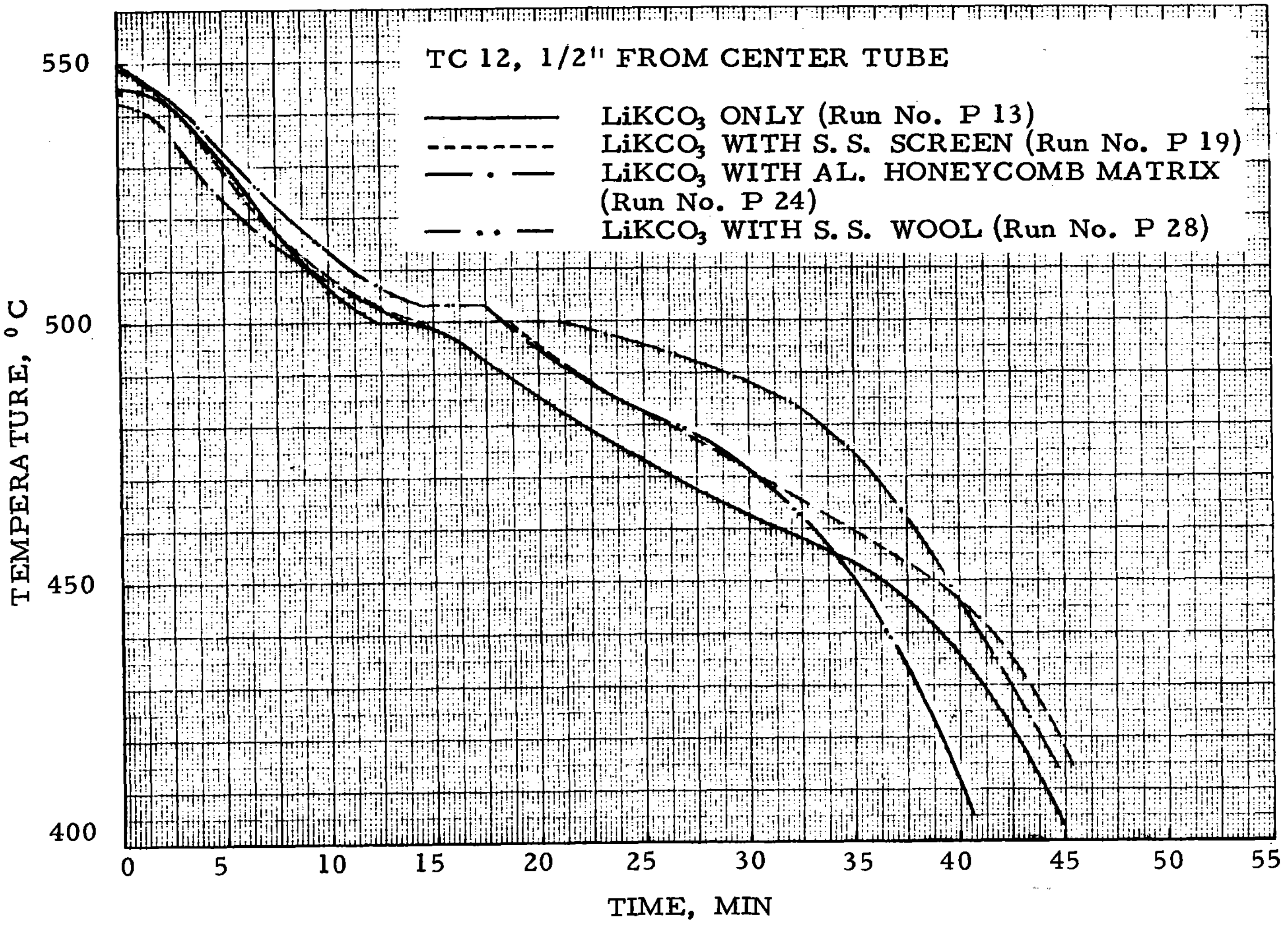

Figure 2.4.4 TEMPERATURE RESPONSES VERSUS TIME AT 1/2-INCH FROM CENTER COOLING TUBE

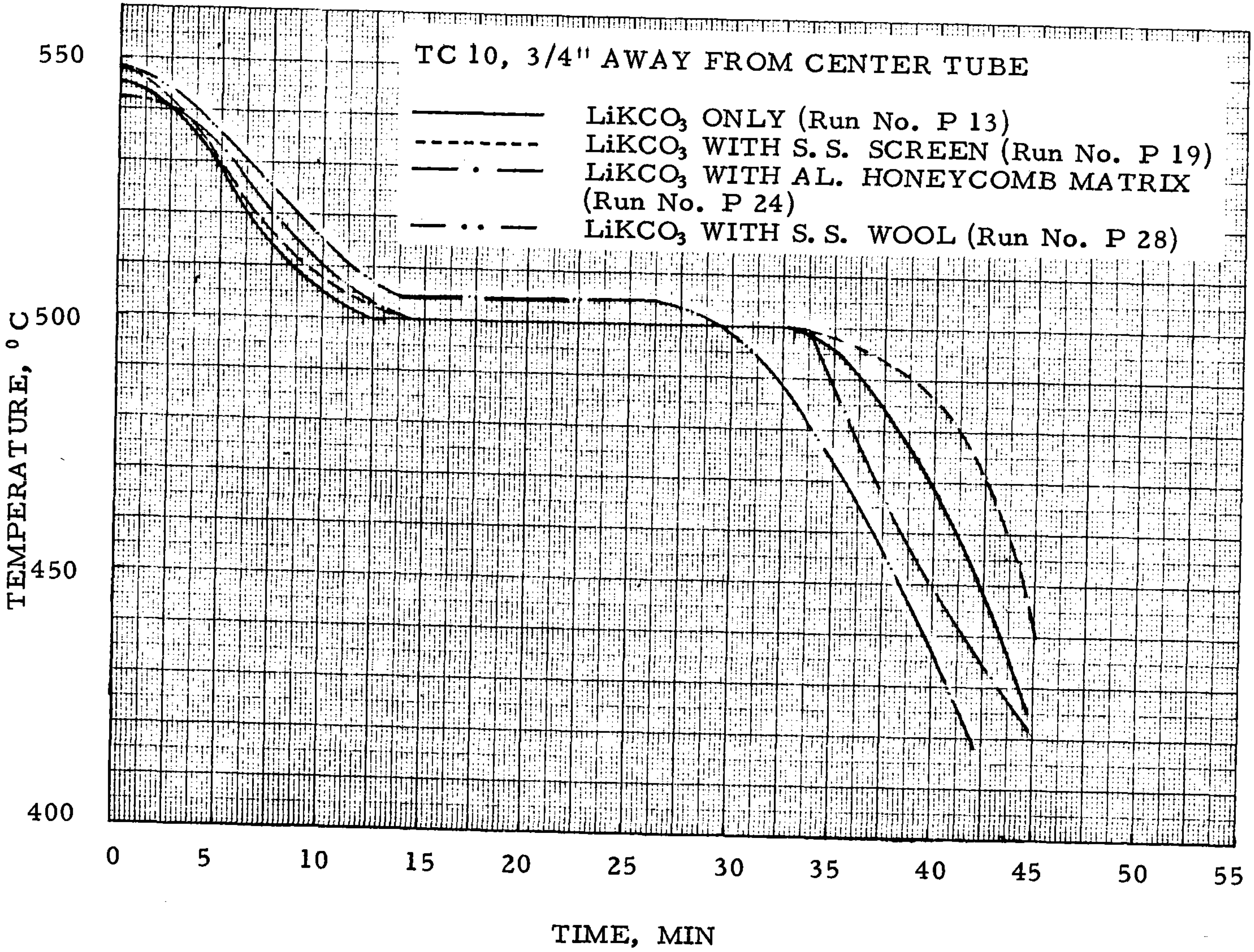

Figure 2.4.5. TEMPERATURE RESPONSES VERSUS TIME AT 3/4-INCH FROM CENTER COOLING TUBE

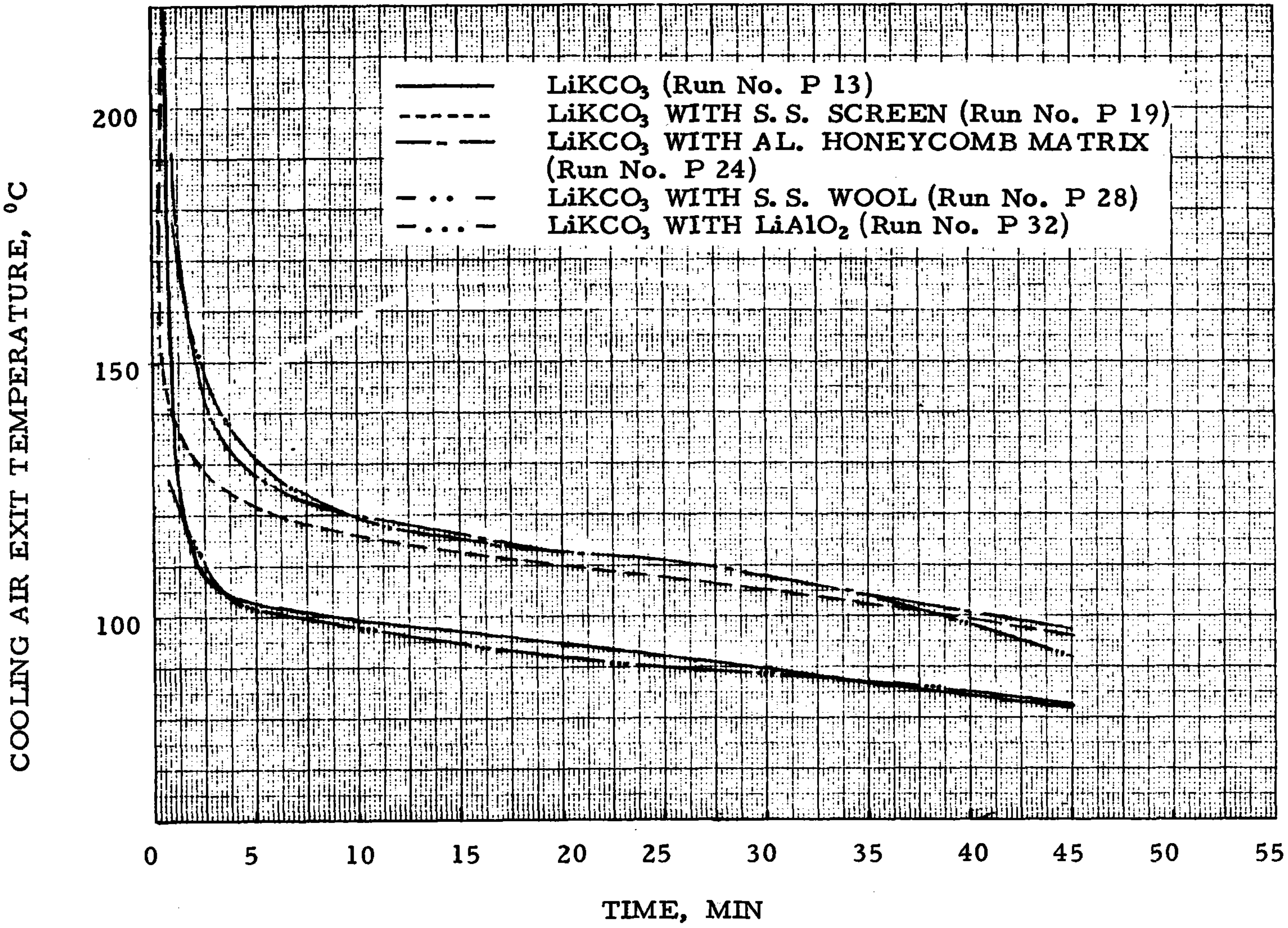

Figure 2.4.6 EXIT AIR TEMPERATURE VERSUS TIME

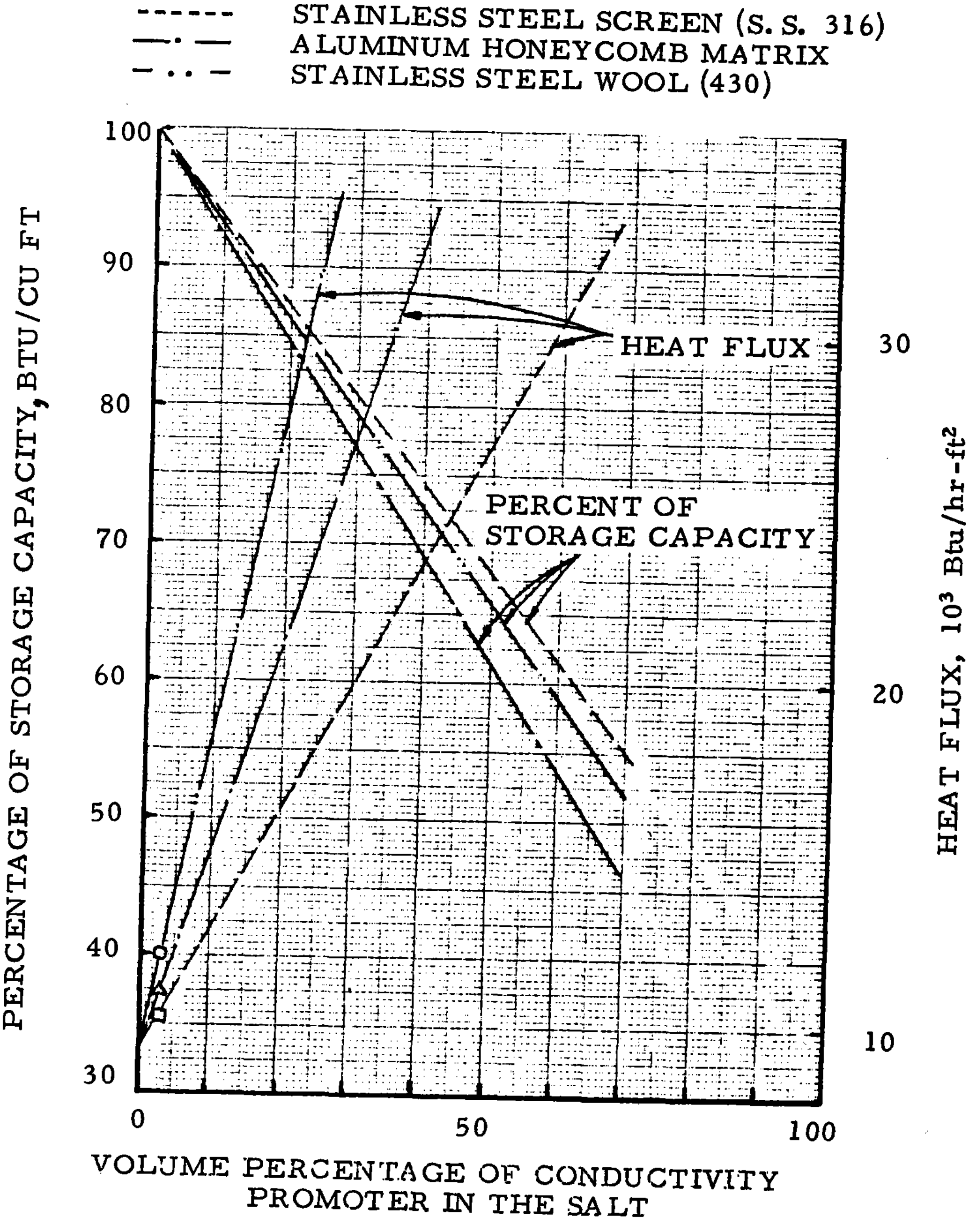

Figure 2.4.7 ESTIMATED EFFECT OF CONDUCTIVITY PROMOTERS ON HEAT FLUX AND STORAGE CAPACITY BETWEEN 450° AND 550° C IN THE PILOT-TES SYSTEM

2.5. CONSTRUCTION MATERIALS

The heat exchanger conduits, the construction materials for containment of the salt, and the conductivity promoters must withstand the corrosive attack of the salt. As we briefly described in our Task I Report on Salt Selection[3], carbonates are relatively less corrosive compared with chlorides, fluorides, sulfates, and phosphates. Molten carbonates are used in fuel cells[15], gasification of coal[20], cleanup of sulfur-containing gases[21], and other applications. A reasonable amount of corrosion data on molten carbonates is, therefore, available. Although specific data for our PCM $LiKCO_3$ is scarce, data on other alkali-metal carbonate mixtures have been reported and we believe that the corrosion behavior of $LiKCO_3$ would be similar to that of the other alkali-metal carbonates. Therefore, in this section we will present all pertinent corrosion data on alkali-metal carbonates. We plan to verify the corrosion data in our experimental TES system, and have begun some initial corrosion measurements under this task. More systematic corrosion data under operating conditions in our TES units will be obtained, and reported in the future reports.

2.5.1. Corrosion Data

Janz and coworkers[22, 23] studied corrosion of Type 304 and 347 stainless steels in the Li_2CO_3-Na_2CO_3-K_2CO_3 ternary eutectic under submerged conditions. Based on their experiments, the authors concluded that both Type 304 and 347 stainless steels passivate under submerged conditions in an oxidizing environment. A corrosion of 10 mils/yr was reported for Type 347 stainless steel in static tests at 730° C. (See Table 2.5.1.)

Davis and Kinnibrugh[24] studied corrosion by the Li_2CO_3-Na_2CO_3 eutectic mixture under fully and partially submerged conditions, and reported a greater corrosion attack under partially submerged conditions. This observation is important for our TES system because a partially submerged condition is likely to occur at the liquid-gas interface at the top of the liquid $LiKCO_3$. Differences in the activity of the oxidizing species in the meniscus area and in the bulk liquid are responsible for the higher degree of corrosion. Experimental verification of the expected greater corrosion will be discussed in Section 2.5.2. Davis and Kinnibrugh also noted that ferro-aluminum alloys, such as Kanthal A, Kanthal Al, and Hoskins 815 were more resistant than the 300-series stainless steels.[24] (See Table 2.5.1.)

Atomics International[20] has employed molten carbonates for sulfur removal and as reaction media for in situ combustion. Detailed studies of corrosion by carbonates under static and dynamic conditions have been carried out at Atomic International. Their melts consisted of the ternary eutectic as well as with additions of 20% sulfide or 20% sulfite melts. Some results of their 50-hour static tests and 1500-hour dynamic corrosion tests at 500° C are summarized in Table 2.5.1. The Atomics International report contains additional data for various alloys and ceramic materials. Their results suggest that—

1. Up to 600° C, Type 347 stainless steel appears to be satisfactory for containing ternary carbonates in the presence or absence of sulfur compounds. A 1-year dynamic test at 500° C showed a corrosion of only 0.2 mils/yr for this stainless steel.
2. At higher temperatures, containment of these melts requires high-chromium alloys, ceramics, cermets, or a frozen skull of the salt.

Corrosion data on various grades of graphites has also been reported by Atomics International (Table 2.5.1). The corrosion rate obtained from 50-hour exposure tests varied from 2 to 150 mils/yr. Graphite is attractive as a conductivity promoter because of its high conductivity, but its corrosion behavior for different grades of interest needs to be investigated.

Aluminum is also a possible candidate for a conductivity promoter because it possesses a high conductivity and can also be considered as a construction material. Aluminum is resistant to carbonates at temperatures up to 600°C[25] and at the Institute of Gas Technology, we have operated molten carbonate fuel cells at 500° to 600°C using aluminum hardware.[25] Noting that the melting point of aluminum is 660°C, the corrosion resistance of aluminum appears remarkable. This is possible because of the formation of a protective alumina layer on the surface, which in turn reacts with carbonates to form a highly protective layer of lithium aluminate.[24]

The TES unit should be designed for periodic (daily) cycles, so data on corrosion of materials under thermal-cycling conditions will be required. Atomics International also studied the effect of thermal cycles on corrosion rates. If the passivated films separate from the substrate during thermal cycles, the corrosion rate is expected to be greater than that found in constant temperature tests. For Haynes 25 and Hastelloy G and X, the corrosion rate was found to be 5 to 20 times greater under thermal cycling.

Table 2.5.1. CORROSION RATES OBSERVED BY VARIOUS INVESTIGATORS

Material	Composition of Carbonates	Gas Environment	Temp, °C	Time, hr	Corrosion Rate, mils/yr	Remarks	Reference
1020 Steel	Ternary eutectic[e]	Air	500	50	4.84	Static test	20
Type 304 L SS	Ternary eutectic	Air	500	50	0.48	Static test	20
		Air	600	50	-4.8[g]	Static test	20
Type 310 SS	52 Li_2CO_3 + 48 Na_2CO_3	$O_2 + CO_2$ (?)	680	--[f]	1.5	● -850 mv, submerged	24
		$O_2 + CO_2$ (?)	680	--[f]	4.2	● -100 mv, submerged	24
	Ternary eutectic	Air	600	50	4.8	Static test	20
Type 321 SS	52 Li_2CO_3 + 48 Na_2CO_3	$O_2 + CO_2$ (?)	680	--[f]	6.9	● -850 mv, submerged	24
		$O_2 + CO_2$ (?)	680	--[f]	7.6	● -100 mv, submerged	24
Type 347 SS	43.5 Li_2CO_3 + 31.5 Na_2CO_3 + 25 K_2CO_3	CO_2	730	95	10	Submerged	22
	52 Li_2CO_3 + 48 Na_2CO_3	$O_2 + CO_2$ (?)	680	--[f]	2.2	● -850 mv,[h] submerged	24
		$O_2 + CO_2$ (?)	680	--[f]	1.3	● -100 mv,[h] submerged	24
	Ternary eutectic	Air	600	50	2.4	Static test	20
		Air	700	50	3.1	Static test	20
		Air	600	1500	0.3	Dynamic test	20
		Air	700	1500	> 90	Dynamic test	20
		Air	500	8000	0.2	Dynamic test	20
Type 430 SS	Ternary eutectic	Air	500	50	2.86	Static test	20
Kanthal A	52 Li_2CO_3 + 48 Na_2CO_3	$O_2 + CO_2$ (?)	680	--[f]	0	● -850 mv[h]	24
	53% $LiAlO_2$ + ternary eutectic	Air (?)	700	1000	0	Wires embedded in a paste mixture	24
Kanthal A-I	52 Li_2CO_3 + 48 Na_2CO_3	$O_2 + CO_2$ (?)	680	--[f]	0	● -850 mv,[h] submerged	24
			700	--[f]	0.16	● -100 mv,[h] submerged	24
Graphite[a]	Ternary eutectic	Air	500	50	2.6	Static test	20
Graphite[b]	Ternary eutectic	Air	500	50	1.8	Static test	20
Graphite[c]	Ternary eutectic	Air	500	50	150	Static test	20
Graphite[d]	Ternary eutectic	Air	500	50	6.2	Static test	20
Alumina	Ternary eutectic	Air	500	50	negligible	Static test	20

[a] AGSX graphite #571X.
[b] Carborundum Metal Pumping Service graphite.
[c] K. B. Bonite graphite.
[d] Raschig ring 571 B.
[e] Ternary eutectic composition is 43.5 mol % Li_2CO_3 + 31.5 mol % Na_2CO_3 + 25 mol % K_2CO_3.
[f] Potentiostatic polarization scans.
[g] Negative sign indicates a weight gain during the test.
[h] Working potential with reference to 67 CO_2 + 33 O_2 reference electrode.

Stress corrosion cracking and the effect of chlorides, sulfides, sulfites, and sulfates under various conditions have also been studied.[21] Sulfur compounds enhanced corrosion, but chloride compounds did not alter the corrosion rate markedly. Therefore, it is desirable to avoid sulfur-bearing impurities in commercial $LiKCO_3$ powder. Higher corrosion rates can be expected if stresses exist in the components.

2.5.2. Corrosion Mechanisms and Thermodynamics

Examination of the outer film of the stainless steels showed[21] that a dense layer of $LiCrO_2$ was formed, which is protective up to 700° C. This conclusion, based on X-ray diffraction and fluorescence studies, is in disagreement with that of Janz and Conte,[22] who reported a $LiFeO_2$ layer as the corrosion product. It is possible that, because the X-ray diffraction patterns of $LiFeO_2$ and $LiCrO_2$ are similar,[20] Janz and Conte could not distinguish between $LiFeO_2$ and $LiCrO_2$. The results of Atomics International using X-ray fluorescence are therefore more reliable. Note that in either case, some loss of Li_2CO_3 can be expected from the initial Li_2CO_3-K_2CO_3 mixture. Because of the relatively large quantities of salt mixture compared with the amount of corrosion products formed, the loss of Li_2CO_3 will be insignificant.

2.5.3. Experimental Observations

The corrosion of two materials was measured during the report period:

1. Type 304 stainless steel tube used for $LiAlO_2$ settling studies, and
2. Aluminum honeycomb in the pilot TES unit.

Type 304 stainless steel tube was used for determining settling rates in $LiKCO_3$ + $LiAlO_2$ mixture at 530° C (Section 2.3). Two metallographic sections were obtained from the tube heated for 1250 hours: 1) in the meniscus area at the top of the tube and 2) in the middle of the tube, where the interior wall of the tube is completely surrounded by the molten salt. Figure 2.5.1 shows a metallograph of the material exposed in the meniscus area, which shows a corrosion of 2 mils in 1250 hours. This is equivalent to 14 mils/yr if a linear corrosion behavior is assumed. However, corrosion behavior is generally parabolic $[\text{corrosion} \propto (\text{time})^{1/2}]$, thus a long-term corrosion rate much lower than 14 mil/yr can be expected. Compared with the observed corrosion in the meniscus area, the corrosion in the interior region was negligible. The observations confirm the differences in corrosion rates reported by Davis and Kinnibrugh[24] for submerged and partially-submerged conditions.

Corrosion of aluminum honeycomb used as a conductivity promoter was observed in a terminated pilot TES test that underwent 5 cycles between 550° C and room temperature. Because the total exposure time was less than 100 hours, the results are only tentative and cannot be extrapolated to predict long-term corrosion. Figure 2.5.2 shows a metallograph of the section where maximal corrosion of the honeycomb was observed. An average corrosion of approximately 0.1 mil can be measured on this metallograph. More long-term corrosion measurements will be performed to obtain reliable values.

In summary, 300-series stainless steels (e.g., Types 304 and 347) appear satisfactory under submerged conditions. A somewhat greater amount of corrosion was observed on Type 304 stainless steel in the meniscus region, but additional tests are necessary to obtain long-term corrosion rates in this region. Aluminum is an acceptable material, provided precautions are taken to prevent high temperatures. Because aluminum is mechanically weak, proper design considerations are required.

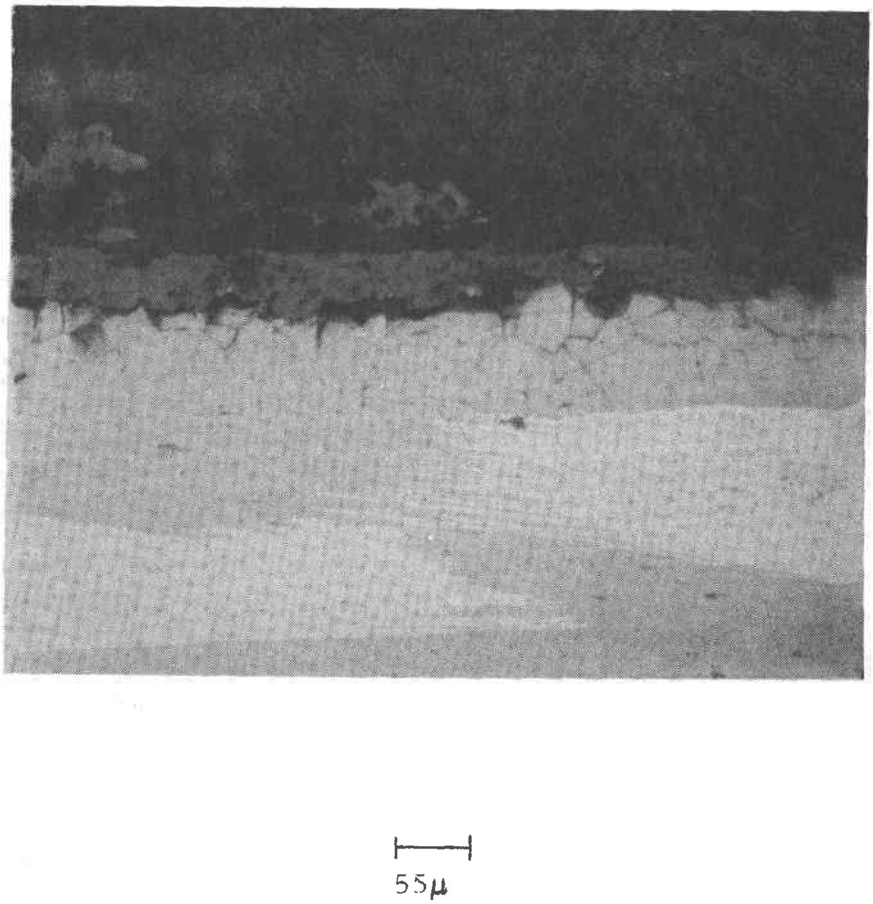

Figure 2.5.1. METALLOGRAPH OF TYPE 304 SS IN THE MENISCUS REGION EXPOSED AT 530° C FOR 1250 HOURS (180 X)

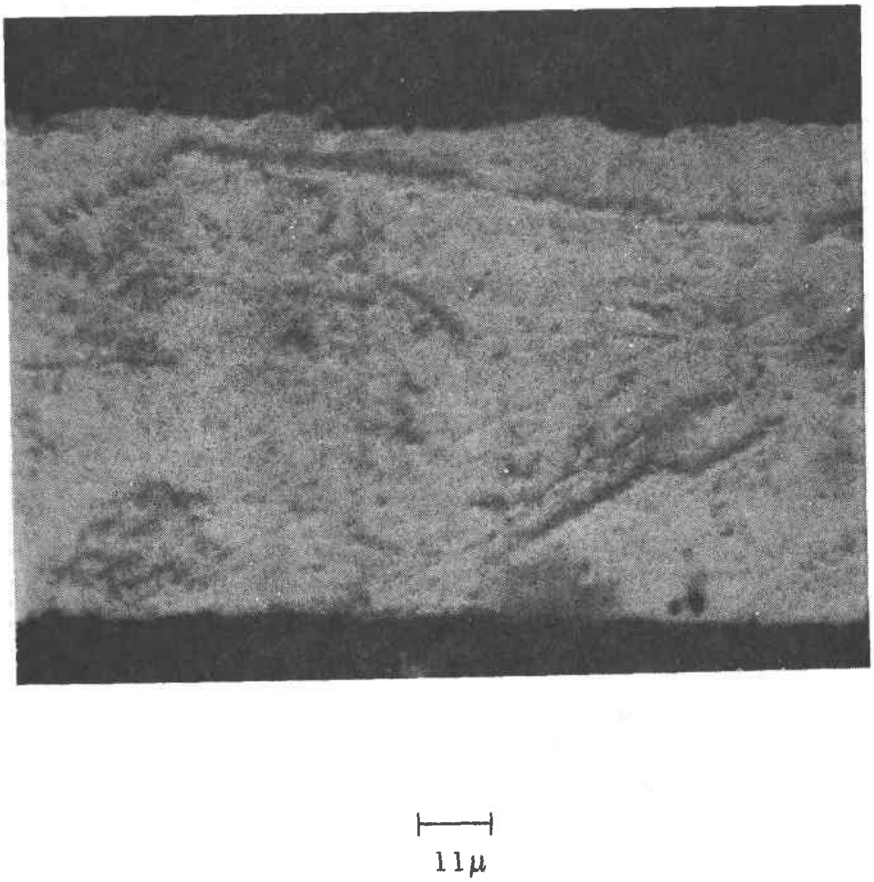

Figure 2.5.2. METALLOGRAPH OF ALUMINUM HONEYCOMB MATRIX AFTER FIVE CYCLES (8 hr/cycle) IN $LiKCO_3$ OPERATING BETWEEN 550^0 C AND ROOM TEMPERATURE (910 X)

2.6. REFERENCES CITED

1. Bramlette, T. T. et al., "Survey of High Temperature Thermal Energy Storage," SAND 75-8063, Livermore, Calif.: Sandia Laboratories, 1976.
2. Megerlin, F., "Geometrically One-Dimensional Heat Conduction During Melting and Solidification," Forsch. im Ingenieniwesen, 34, No. 2 (1968) (German Text).
3. Maru, H.C., Dullea, J. and Huang, V. M., "Molten Salt Thermal Energy Storage Systems: Salt Selection, Topical Report, ERDA Contract No. E(11-1)-2888, Institute of Gas Technology, Chicago, August 1976.
4. Carslaw, H. S. and Jaeger, J. C., Conduction of Heat in Solids, 2nd Ed., London: Oxford Univ. Press, 1959.
5. Institute of Fuel, Waste-Heat Recovery, London: Chapman and Hall, Ltd., London, p. 73, 1963.
6. Kardas, A., "On a Problem in the Theory of the Undirectional Regenerator," Int. J. Heat Mass Trans. 9, p. 573, 1966
7. Groeber, H., Forschungsarb. Heft 300, V.D.I., Berlin, 1928.
8. Kreith, F., Principles of Heat Transfer, Scranton, Pa.: Intern. Textbook Co., p. 347, 1959.
9. Hatch, J. E., et al., "Graphical Presentation of Difference Solutions for Transient Radial Heat Conduction in Hollow Cylinders with Heat Transfer at the Inner Radius and Finite Slabs with Heat Transfer at One Boundary," NASA TR R-56, p. 34, 1960.
10. Chandrasekhar, S., Hydrodynamic and Hydromagnetic Stability, London: Oxford Univ. Press, 1961.
11. Atthey, D. R., "A Finite Difference Scheme for Melting Problems Based on the Method of Weak Solutions," in Moving Boundary Problems in Heat Flow and Diffusion, J. R. Ockenden and W. H. Hodgkins, Eds., Oxford: Clarendon Press, 1975.
12. Janz, G. J., Lorenz, M.R., "Solid-Liquid Phase Equilibria for Mixtures of Lithium, Sodium, and Potassium Carbonates," J. Chem. Eng. Data 6 (3) 321-23, (1961) July.
13. Reshetnikov, N.A. and Perfil'eva, O.G., Russ. J. Inorg. Chem., 13 (6), 870 (1968).
14. Spedding, P. L., "Densities and Molar Volumes of Molten Alkali Carbonate Binary Mixtures," J. Electrochem. Soc., 117 (2), 177-83, (1970) February.
15. Maru, H. C. et al., "Fuel Cell Research on Second-Generation Molten Carbonate Systems, Vol II: Characteristics of Carbonate Melts," Quarterly Progress Report, Argonne National Laboratory Contract No. 31-109-38-3552, Institute of Gas Technology, Chicago, July 1 - September 30, 1976.

16. Broers, G.H.J. and Van Ballegoy, H.J.J., "Phase Equilibria in Li-Na-K Carbonate-Aluminate Systems." Paper presented at the 3rd International Symposium on Fuel Cells, Brussels, June 1969.

17. Mason, D.M. and Van Drunen, C.J., "Production of Beta-Lithium Aluminate," U.S. Patent 3,998,939 (1976) December 21.

18. Perry, R.H. and Chilton, C.H., Eds., Chemical Engineers Handbook, 5th Ed., 3-241, New York: McGraw Hill, 1975.

19. Powers, A. E., "Conductivity in Aggregates," U.S. Atomic Energy Commission Contract No. W-31-109 Eng-52 1961.

20. Atomics International, "Development of a Molten Carbonate Process for Removal of Sulfur Dioxide From Power Plant Stack Gases," Progress Report No. 2 to U.S. Public Health Service Contract No. PH 86-67-128. Canoga Park, Calif., 1968.

21. Grantham, L. F. and Ferry, P. B., "Corrosion in Alkali Carbonate Based Melts," Abstract No. 391 in Extended Abstracts, Vol 76-1 for the 149th Meeting of the Electrochemical Society, Washington, D.C., May 2-7, 1976.

22. Janz, G.J. and Conte, A., "Corrosion of Gold-Palladium, Nickel and Type-347 Stainless Steel in Molten Alkali Carbonates," Corrosion 20, 237t - 238t (1964).

23. Janz, G.J. and Conte, A., "Potentiostatic Polarization Studies in Fused Carbonates. II. Stainless Steel," Electrochim Acta, 9, 1279-1287 (1964).

24. Davis, H.J. and Kinnibrugh, D.R., "Passivation Phenomena and Potentiostatic Corrosion in Molten Alkali Metal Carbonates," J. Electrochem. Soc. 117 (3), 392-396 (1970).

25. Institute of Gas Technology, "Development of Molten Carbonate Fuel Cells," A.G.A. Project DC-4-1. Final Report, Chicago, 1967.

NOMENCLATURE

A = heat transfer area, sq ft, sq in.

a = characteristic thickness, ft, in.
(half-thickness of a slab, radius of a cylinder or a sphere)

C = a coupling coefficient, (def. in Equation 2.2.17)

c_p = heat capacity, Btu/lb_m - °F

d = wall thickness, ft
tube diameter, ft, in.

G = mass velocity, lb_m/hr-sq ft

h = surface heat transfer coefficient, Btu/hr-sq ft- °F

ΔH_f = heat of fusion, Btu/lb_m

i = enthalpy, specific enthalpy, Btu, Btu/lb_m
also, $i = \sqrt{-1}$

k = thermal conductivity, Btu/hr-ft- °F

K = wave number, ft^{-1}

L = significant dimension, ft

M = dimensionless frequency; $M = \sqrt{\frac{\pi a^2 \nu}{\alpha}} = \sqrt{\frac{\pi}{N_{Fo}{}^0}}$

m = total mass, lb_m

$\dot{m}$ = mass flow rate, lb_m/hr

N_{Fo} = Fourier number (dimensionless time); $N_{Fo} = \alpha\tau / a^2$

N^0_{Fo} = dimensionless period; $N^0_{Fo} = \alpha\tau_o / a^2$

N_{Nu} = Nusselt number (ratio of surface conductance to fluid conductance);
$N_{Nu} = ha/k_f$

N_{ph} = phase change number (ratio of heat of fusion to the sensible heat between the melting point and a reference temperature);
$N_{ph} = \Delta H_f \rho_\ell / C_{ps}(t_m - t_a)\rho_s$

N_{Pr} = Prandtl number (ratio of kinematic viscosity to thermal diffusivity);
$N_{Pr} = \nu/\alpha$

N_{Ra} = Rayleigh number (ratio of buoyant to thermal forces)

N_{Re} = Reynolds number (ratio of inertial to viseous forces);
$N_{Re} = vd/\nu$

N_{Bi} = Biot number (ratio of surface conductance to interior solid conductance);
$N_{Bi} = ha/k_s$ or Ua/k_s.

p = perimeter, ft, in.

R = r/r_o, radius ratio

r = radial coordinate, ft

Q, q = quantity of heat, Btu

t = temperature, °C, °F

T = absolute temperature, °R

U = overall heat transfer coefficient, Btu/hr-sq ft-°F

u = utilization factor; $u = \Pi / \Lambda$

V = fluid volume, cu ft

v = velocity, ft/hr

X = moving length coordinate, ft

x = length coordinate, ft

z = longitudinal coordinate, direction of fluid flow, ft

<u>Greek Letters</u>

α = thermal diffusivity, sq ft/hr; $\alpha = k/c_p \rho$

β = coefficient of volume expansion, $°R^{-1}$; $\beta = \rho_\infty - \rho / \rho \Delta T$

δ = a finite difference operator

Δ = same as δ

ϵ = temperature increment above and/or below the melting point, °C, °F

η = thermal recovery (a temperature excess ratio)

θ = dimensionless temperature ratio; $|\theta| = 1$

Λ = reduced length; $\Lambda = \dfrac{h(A/V)z}{c_{pf}G}$

λ = wavelength, ft

μ = dynamic viscosity, lb_f-hr/sq ft, centipoise

ν = kinematic viscosity, sq ft/hr
frequency, cps

Π = reduced time; $\Pi = \dfrac{hA\tau}{c_pM}$

ρ = density, lb_m/cu ft

τ = time

τ_0 = period

φ = frequency-dependent storage function

ω = circular frequency, rad/s; $\omega = 2\pi\nu$

<u>Subscripts</u>

a = ambient

app = apparent

f = fluid

in = initial

ins = insulation

ℓ = liquid (phase)

m = melting

s = solid (phase)

surf = surface

w = wall

<u>Superscripts</u>

' = per unit length

'' = per unit area

''' = per unit volume

• = per unit time

*U.S.GOVERNEMNT PRINTING OFFICE: 1977-740-062/ 93 REGION NO. 4